

New Evidence for Extended He II Reionization at $z \gtrsim 3.5$ from He II Lyman Alpha and Beta Transmission Spikes *

KIRILL MAKAN ¹, GÁBOR WORSECK ¹, FREDERICK B. DAVIES ^{2,3,4}, JOSEPH F. HENNAWI ², J. XAVIER PROCHASKA ⁵,
AND PHILIPP RICHTER ¹

¹*Institut für Physik und Astronomie, Universität Potsdam, Karl-Liebknecht-Str. 24/25, D-14476 Potsdam, Germany*

²*Department of Physics, University of California, Santa Barbara, CA 93106-9530, USA*

³*Lawrence Berkeley National Laboratory, 1 Cyclotron Rd., Berkeley, CA 94720-8139, USA*

⁴*Max-Planck-Institut für Astronomie, Königstuhl 17, D-69117 Heidelberg, Germany*

⁵*University of California Observatories, Lick Observatory, University of California, Santa Cruz, CA 95064, USA*

(Received 2020 December 14; Revised 2021 March 9; Accepted 2021 March 10)

ABSTRACT

We present new high-resolution ($R = \lambda/\Delta\lambda \sim 14,000$) spectra of the two brightest He II-transparent quasars in the far-UV (FUV) at $z_{\text{em}} > 3.5$, HE2QS J2311–1417 ($z_{\text{em}} = 3.70$) and HE2QS J1630+0435 ($z_{\text{em}} = 3.81$), obtained with the Cosmic Origins Spectrograph (COS) on the *Hubble Space Telescope* (HST). In the predominantly saturated He II absorption spectra, both sightlines show several isolated resolved (full width at half maximum FWHM $\gtrsim 50 \text{ km s}^{-1}$) transmission spikes in He II Ly α and He II Ly β . The incidence of such spikes decreases with increasing redshift, but both sightlines show significant spikes at $z \gtrsim 3.5$, signaling the presence of fully ionized regions in the $z \gtrsim 3.5$ intergalactic medium (IGM). We employ an automated algorithm to compare the number of detected He II transmission spikes to predictions from mock spectra created from the outputs of a cubic (146 cMpc)³ optically thin N_YX hydrodynamical simulation, assuming a range of UV background photoionization rates $\Gamma_{\text{He II}}$. From the incidence of Ly α and Ly β transmission spikes we infer similar photoionization rates of $\Gamma_{\text{He II}} = (2.0^{+0.6}_{-0.5}) \times 10^{-15} \text{ s}^{-1}$ at $3.51 < z < 3.66$ and $\Gamma_{\text{He II}} = (0.9 \pm 0.3) \times 10^{-15} \text{ s}^{-1}$ at $3.460 < z < 3.685$, respectively. Because the transmission spikes indicate fully ionized regions at $z \gtrsim 3.5$ along both lines of sight, our observations provide further evidence that He II reionization had substantially progressed at these redshifts.

Keywords: Cosmic background radiation (317); Hubble Space Telescope (761); Intergalactic medium(813); Quasar absorption line spectroscopy (1317); Reionization (1383); Ultraviolet astronomy (1736)

1. INTRODUCTION

The epoch of helium reionization, when helium lost its second electron, was the last major phase transition in the intergalactic medium (IGM). While hydrogen reionization was substantially complete by $z \sim 6$ (Fan et al. 2006; Bosman et al. 2018; Eilers et al. 2018; Planck Collaboration et al. 2018; Bañados et al. 2018; Davies et al. 2018) and might have lasted until $z \sim 5.2$ (Becker et al. 2015; Kulkarni et al. 2019a; Nasir & D’Aloisio 2020; Keating et al. 2020b; Choudhury et al. 2021), helium was fully ionized later at $z \sim 3$ due to the required hard UV photons ($E \geq 54.4 \text{ eV}$) that could only

be provided by quasars (e.g., Madau & Meiksin 1994; Fardal et al. 1998; Miralda-Escudé et al. 2000; Sokasian et al. 2002; Furlanetto & Oh 2008; McQuinn et al. 2009; Compostella et al. 2013, 2014). The timing and spatial morphology of helium reionization is of great interest to observational cosmology, because it determines the spatial variations in amplitude and spectral shape of the high-redshift UV background (e.g., Furlanetto & Dixon 2010; Davies et al. 2017; Meiksin 2020), and it constrains the contribution of quasars to it (e.g., Compostella et al. 2014; Garaldi et al. 2019a; Puchwein et al. 2019; Kulkarni et al. 2019b).

In particular, extended photoheating during the helium reionization epoch governs the thermal evolution of the IGM at $z < 6$ (e.g., McQuinn et al. 2009; Compostella et al. 2013, 2014; Oñorbe et al. 2017; La Plante et al. 2017; Puchwein et al. 2019). Measurements of the IGM temperature at mean density obtained from the H I Ly α forest with a variety of techniques show gradual heating at $z < 4.5$ (Becker et al. 2011; Boera et al. 2014, 2019) with a broad temperature maximum at $2.8 \lesssim z \lesssim 3.4$ (e.g., Ricotti et al. 2000; Schaye et al.

Corresponding author: Kirill Makan
kmakan@astro.physik.uni-potsdam.de

* Based on observations made with the NASA/ESA *Hubble Space Telescope*, obtained at the Space Telescope Science Institute, which is operated by the Association of Universities for Research in Astronomy, Inc., under NASA contract NAS5-26555. These observations are associated with program 15356.

2000; Lidz et al. 2010; Boera et al. 2014; Hiss et al. 2018; Walther et al. 2019). This temperature evolution is consistent with an extended He II reionization epoch ending at $z \sim 3$ (Puchwein et al. 2019).

Direct evidence for delayed extended He II reionization can be gained from intergalactic He II Lyman series absorption against $z > 2$ quasars in the FUV from space (e.g., Miralda-Escude 1993; Madau & Meiksin 1994; Jakobsen et al. 1994). However, the fraction of quasars showing emission at the He II Ly α rest-frame wavelength $\lambda_\alpha = 303.7822 \text{ \AA}$ strongly decreases with increasing redshift due to the declining quasar luminosity function and increasing cumulative H I Lyman continuum absorption (Møller & Jakobsen 1990; Picard & Jakobsen 1993; Worseck & Prochaska 2011). Wide-field FUV photometry obtained with the *Galaxy Evolution Explorer* (GALEX; Martin et al. 2005; Morrissey et al. 2007) enabled the selection of likely He II-transparent sightlines (Syphers et al. 2009a,b; Worseck & Prochaska 2011). But only the FUV-brightest of these allow for efficient follow-up with *HST*'s Cosmic Origins Spectrograph (COS; Green et al. 2012) at a data quality sufficient for quantitative measurements of intergalactic He II absorption (Worseck et al. 2011; Syphers et al. 2012; Worseck et al. 2016, 2019, hereafter W19).

To date, science-grade (signal-to-noise ratio $S/N \gtrsim 3$) *HST* spectra of 25 He II sightlines sample the redshift evolution of the large-scale (~ 40 comoving Mpc) He II Ly α absorption at $2.3 \lesssim z \lesssim 3.8$ (e.g., Reimers et al. 1997; Heap et al. 2000; Shull et al. 2010; Syphers & Shull 2013, 2014; Worseck et al. 2011, 2016, W19). The small sightline-to-sightline variance in the measured effective optical depth τ_{eff} at $z \lesssim 2.7$ is consistent with expectations from IGM density fluctuations and a spatially uniform UV background, marking the end of the He II reionization epoch at $z \simeq 2.7$ (Worseck et al. 2011; W19). At higher redshifts, the increasing τ_{eff} variations are compatible with increasing UV background fluctuations in a still predominantly ionized IGM with a median volumetric He II fraction of $x_{\text{HeII}} \simeq 0.025$ at $z \simeq 3.1$ (Worseck et al. 2016; Davies et al. 2017; W19). However, beyond the tail end of He II reionization, the constraints at $z > 3.3$ are limited by the decreasing sample size and saturation in He II Ly α at the sensitivity limit of *HST*/COS (W19).

Higher-order Lyman series absorption can provide additional constraints on the reionization history due to higher saturation limits, e.g. for Ly β $\tau_\beta(z) \simeq 0.16\tau_\alpha(z)$. This has been exploited extensively to probe to higher H I fractions at $z > 5.5$ (Becker et al. 2001; White et al. 2003; Fan et al. 2006; Gallerani et al. 2006; Becker et al. 2015; McGreer et al. 2015; Davies et al. 2018; Eilers et al. 2019; Nasir & D'Aloisio 2020; Keating et al. 2020a; Yang et al. 2020). For the measured effective optical depths the above conversion does not apply, but instead depends on the IGM density structure (e.g. Oh & Furlanetto 2005; Fan et al. 2006) and its thermal state (e.g. Furlanetto & Oh 2009; Eilers et al. 2019). Moreover, Ly β absorption is entangled with foreground Ly α absorption at $z_{\text{fg}} = (1+z_\beta)\lambda_\beta/\lambda_\alpha - 1$ that is best accounted for by appropriate forward-modeling (Eilers et al. 2019; Keating

et al. 2020a). Analogously, He II Ly β absorption enables one to improve the constraints on the He II fraction by a factor of ~ 3 to $x_{\text{HeII}} \gtrsim 0.1$, particularly in underdense regions identified in the co-spatial H I Ly α forest (McQuinn 2009). However, due to low UV instrument sensitivity in the wavelength range of interest, He II Ly β observations have been challenging (Zheng et al. 2004; Syphers et al. 2011). Additionally, the inferred He II Ly α effective optical depths at $2.7 \lesssim z \lesssim 3.4$ strongly depend on the uncertain modeling of foreground Ly α absorption, resulting in constraints similar to the direct He II Ly α measurements (Syphers et al. 2011).

Besides the mean large-scale IGM absorption, several additional statistics have been used to probe the H I reionization history with H I absorption spectra, such as the length of continuous low-transmission regions (so-called dark gaps, Songaila & Cowie 2002; Paschos & Norman 2005; Fan et al. 2006; Gallerani et al. 2006, 2008; Gnedin et al. 2017) and the properties of isolated transmission spikes between these regions (Gallerani et al. 2006, 2008; Gnedin et al. 2017; Barnett et al. 2017; Chardin et al. 2018; Garaldi et al. 2019b; Gaikwad et al. 2020; Yang et al. 2020). While these statistics provide an intuitive feature decomposition of the high-redshift Ly α absorption, inferences on the reionization epoch require detailed forward-modeling of simulated spectra to match the spectral resolution and noise properties of the data (e.g., sky line residuals for dark gaps). Extension to Ly β is complicated by foreground Ly α modeling and numerical convergence in underdense regions, although the Ly β dark gap distribution may discriminate between H I reionization scenarios (Nasir & D'Aloisio 2020). Analogously, the He II Ly α dark gap and transmission spike distributions have been suggested as powerful diagnostics to distinguish He II reionization models (Compostella et al. 2013), but have not been rigorously applied due to limited high-quality data for just two well-studied He II sightlines at $z \sim 2.8$ and 3.2 (Reimers et al. 1997; Heap et al. 2000; Smette et al. 2002; Shull et al. 2010; Syphers & Shull 2014).

Here we present new high-resolution ($R \sim 14,000$) He II Ly α and Ly β absorption spectra of the two FUV-brightest quasars at $z_{\text{em}} > 3.5$, which have been discovered and analyzed at low spectral resolution by W19. These two rare¹ quasars, HE2QS J1630+0435 ($z_{\text{em}} = 3.81$) and HE2QS J2311-1417 ($z_{\text{em}} = 3.70$), are the only two quasars at $z_{\text{em}} > 3.5$ that are bright enough to be observed with the high-resolution *HST*/COS G130M grating. The high-quality data and a new automated transmission spike measurement algorithm allow us to infer new constraints for the late stages of the He II reionization epoch. This paper is structured as follows. In Section 2 we describe the observations and our custom data reduction. In Section 4 we present our methods to detect He II transmission spikes. Comparing the number of observed transmission spikes to outputs from numerical

¹ Worseck & Prochaska (2011) estimated that just ~ 10 $z_{\text{em}} > 3.5$ quasars are detectable with GALEX at FUV $\lesssim 21.5$ on the full sky, and thus accessible to *HST*.

Table 1. *HST*/COS G130M observational data.

Object	Data set	Date	t_{exp} (s)	λ_{cent} (Å)
HE2QS J1630+0435	ldm601010	2018 Jun 13	5832	1291
	ldm603010	2018 Jul 8	11053	1327
	ldm602010	2018 Jul 11	11041	1222
	ldm602020	2018 Jul 11	2916	1291
	ldm604010	2018 Jul 13	2304	1327
	ldm625010	2018 Jul 24	5234	1291
	ldm6h5020	2018 Jul 31	2914	1327
	ldm6h6010	2018 Aug 13	2318	1291
	ldm6h7010	2018 Aug 21	2303	1327
HE2QS J2311–1417	ldm605010	2018 Sep 13	12742	1291
	ldm608010	2018 Sep 14	10044	1327
	ldm607010	2018 Sep 15	10040	1222
	ldm609010	2018 Sep 22	7360	1327
	ldm606010	2018 Sep 27	12742	1291
	ldm6h8010	2018 Nov 5	1992	1327

simulations we then infer the He II photoionization rate (Section 5). Finally, we summarize in Section 6.

We use a flat cold dark matter cosmology with dimensionless Hubble constant $h = 0.685$ ($H_0 = 100h \text{ km s}^{-1} \text{ Mpc}^{-1}$) and density parameters $(\Omega_m, \Omega_b, \Omega_\Lambda) = (0.3, 0.047, 0.7)$, consistent with Planck Collaboration et al. (2018).

2. OBSERVATIONS AND DATA REDUCTION

2.1. *HST*/COS G130M Observations

In *HST* Cycle 25 we observed HE2QS J1630+0435 and HE2QS J2311–1417 with the COS G130M grating for 45,915 s and 54,920 s, respectively (Program 15356, PI Worseck). The observations were carried out at COS detector Lifetime Position 4 at three central wavelength settings (1222 Å, 1291 Å, 1327 Å) to provide a continuous wavelength coverage from 1070 Å to 1470 Å at a resolving power of $R = 10,000$ – $17,000$ that varies with wavelength and the different settings. The observations were specifically scheduled to maximize the observation time spent in the Earth’s shadow to reduce the contamination by geocoronal emission lines. Both targets were observed within ~ 1 month (except repeat observations due to guide star acquisition failures) to minimize the impact of quasar variability. Table 1 lists the successfully observed *HST* data sets.

2.2. Data Reduction

The data were reduced using the CALCOS pipeline (v3.3.5) wrapped by our custom python code FaintCOS². The code builds on the procedures of Worseck et al. (2016) and W19, but with improved boxcar trace definition and flat-fielding. In contrast to CALCOS, FaintCOS accurately subtracts the dark current using dark frames, applies custom limits to the detector pulse height amplitude (PHA), adopts narrower extraction apertures that are adequate for point sources,

and co-adds sub-exposures preserving the Poisson counts. FaintCOS provides a streamlined science-grade reduction of Poisson-limited *HST*/COS FUV spectra in a single software environment. Reduction parameters can be tailored to the science objectives. FaintCOS is described in detail in Appendix A.

In addition, we checked the science extraction apertures for occasional transient detector hotspots with a typical width of a few pixels that might mimic He II transmission spikes. We identified these hotspots in stacked dark frames taken around the same time as the science data. The corresponding detector positions were masked in the science data, because hotspots cannot be removed with our dark current subtraction procedure. Although their overall effect is small for our data taken at several central wavelengths and focal-plane offset positions, custom masking of hotspots is required for the faintest COS targets such as ours.

Because of the expected narrow flux spikes in our data, wavelength alignment of different COS setups is essential. Comparing spectra of the calibration star AV 75 (Program 15385) taken at different central wavelengths, we found a distortion in the CALCOS wavelength calibration of up to 0.2 Å (2 resolution elements) at the short wavelength edges (300 pixels) of both FUV detector segments. This is likely due to an imperfect correction of geometrical distortion. We did not manually flag these regions because there is no significant flux detected, neither in individual *HST* data sets, nor in the co-added spectra. Conversely, current COS data showing unsaturated absorption lines in these regions should be checked carefully.

Custom PHA ranges specific to the science data allow for the suppression of the detector dark current (Worseck et al. 2016). From the PHA distributions of geocoronal emission lines and the quasar continuum redward of He II Ly α we inferred $2 \leq \text{PHA} \leq 12$. Our custom boxcar extraction apertures and PHA limits result in a $\sim 60\%$ reduction of the dark current with respect to the default CALCOS procedure.

The dark current in the science extraction apertures was estimated from post-processed dark frames taken within two months around the observation date. To match the orbital environmental conditions during the science observations, the dark frames were restricted to those with a Kolmogorov–Smirnov test statistic $D < 0.03$ between the respective PHA distributions in unilluminated detector areas (Appendix A). The D limit was increased until at least 5 matching dark frames were found. The exposures at the central wavelength 1222 Å had been taken at a higher voltage level on detector segment B, which had not been included in the COS dark monitoring programs 14940 and 15533. Because the dark current depends on the detector voltage, we acquired specific dark frames at the matching segment B voltage to ensure a percent-level accurate dark subtraction for

² <https://github.com/kimakan/FaintCOS>

these data³. Our improved dark current subtraction method has a negligible systematic error of $\leq 0.5\%$ and a random error of $\lesssim 5\%$ (Appendix B).

Although the dark current is the dominant background component, the diffuse UV sky background and scattered geocoronal Ly α emission may not be negligible (Worseck et al. 2016). The diffuse UV sky background was subtracted by using GALEX data (Murthy 2014) as described in Worseck et al. (2016). The subtracted fluxes are small ($f_{\lambda, \text{sky}} \sim 10^{-18} \text{ erg cm}^{-2} \text{ s}^{-1} \text{ \AA}^{-1}$), and correspond to 2–12% of the estimated dark current. Additionally, we inspected both co-added spectra for resolved H₂ fluorescence lines (Sternberg 1989) which can mimic He II transmission spikes. Since even the strongest lines are not present, we conclude that H₂ fluorescence is negligible along these two sightlines and that the sky background is continuous.

Contamination by geocoronal emission lines was suppressed by considering data taken during orbital night (Sun altitude $\leq 0^\circ$) in the affected wavelength ranges. During orbital night, O I $\lambda 1304$ and N I $\lambda 1200$ are very weak or even negligible, depending on the geomagnetic latitude, solar activity, and HST’s orientation to the Sun. The affected spectral regions in the co-added data were replaced with night-only data to suppress these lines below the detection limit (Appendix C). Additionally, we checked for scattered geocoronal Ly α emission by comparing the day-only and night-only fluxes in four saturated regions close to Ly α . The fluxes are either statistically insignificant ($f_\lambda < 3 \times 10^{-18} \text{ erg cm}^{-2} \text{ s}^{-1} \text{ \AA}^{-1}$ at 2σ) or within the systematic error of the dark current, such that scattered light is considered negligible.

The sub-exposures per object were co-added and calibrated in count space to preserve their Poisson statistics, binning to $0.04 \text{ \AA pixel}^{-1}$, corresponding to 2–3 pixels per resolution element. Because the resolution varies with wavelength and G130M central wavelength, we quote for the merged spectra $R \sim 14,000$ at $\lambda \sim 1300 \text{ \AA}$. Statistical Poisson errors for the background-subtracted flux were calculated using the approach of Feldman & Cousins (1998). The resulting Poisson S/N is ~ 3 per pixel in the continuum near He II Ly α in the quasar rest frame, but strongly varies with wavelength due to the different pixel exposure times and He II absorption.

2.3. Continuum Definition

To correct the co-added spectra for Galactic extinction we used the line-of-sight selective extinction $E(B - V)$ from Schlegel et al. (1998) and the extinction curve derived by Cardelli et al. (1989) assuming the Galactic average ratio between the total V band extinction and selective extinction $R_V = 3.1$.

Since both G130M spectra cover only a short part of the quasar continuum redward of He II Ly α , which makes con-

Table 2. Flux Ratio for G140L Spectra at Different Epochs.

Object	1st Epoch	2nd Epoch	Mean Flux Ratio (2nd/1st epoch)
HE2QS J2311–1417	2015 Nov 7	2018 Sep 22	1.02 ± 0.03
HE2QS J1630+0435	2013 Apr 12	2018 Jul 31	0.87 ± 0.02

tinuum fitting impossible, we used the power-law continua derived by W19. In order to correct for intrinsic quasar variability between the two observational epochs, we re-observed each quasar with the G140L grating during one of the G130M visits. Exposure times were 2,182 s for HE2QS J1630+0435 and 2,558 s for HE2QS J2311–1417, respectively. We reduced the G140L data with the same techniques as we did for the G130M exposures and additionally corrected for scattered geocoronal Ly α emission (Worseck et al. 2016). In the G140L spectra we calculated the mean flux redward of He II Ly α emission in 20 \AA bins ($1430\text{--}1730 \text{ \AA}$ for HE2QS J2311–1417 and $1460\text{--}1730 \text{ \AA}$ for HE2QS J1630+0435). For both quasars the flux ratio between the epochs does not depend on wavelength. We adopted the mean flux ratios and their standard errors to scale the W19 continua and their 1σ uncertainties (Table 2).

3. TWO HIGH-RESOLUTION HE II ABSORPTION SPECTRA PROBING $Z > 3.5$

3.1. General Overview

Figure 1 shows the reduced G130M spectra of both quasars with $0.04 \text{ \AA pixel}^{-1}$ and $0.24 \text{ \AA pixel}^{-1}$ binning (under-sampled for visualization). Both spectra cover a short wavelength range of the quasar continuum longward of He II Ly α in the quasar rest frame. The quasar redshifts have been measured by Khrykin et al. (2019), using the C IV and H β emission lines for HE2QS J2311–1417 and HE2QS J1630+0435, respectively. The residual flux immediately shortward of He II Ly α and He II Ly β ($\lambda_\beta = 256.317 \text{ \AA}$) is due to the highly ionized He II quasar proximity zones (Khrykin et al. 2019), which were excluded from further analysis.

The remaining spectral range is covered by predominantly saturated intergalactic He II Lyman series absorption. Both sightlines show long He II Ly α Gunn-Peterson troughs (Gunn & Peterson 1965) with occasional transmission features (i.e., at 1255 \AA and 1390 \AA toward HE2QS J1630+0435). The enhanced scatter at $1270 \text{ \AA} < \lambda < 1290 \text{ \AA}$ is due to the short exposure time in the G130M 1222 \AA setup covering this wavelength range. The spectral range shortward of He II Ly β in the quasar rest frame shows overlapping intergalactic high-redshift He II Ly β and low-redshift foreground He II Ly α absorption. Due to the increasing contamination and low S/N we excluded the He II Ly γ troughs from further analysis.

3.2. Resolved He II Transmission Spikes

³ Reduction with the standard dark monitoring data resulted in a 10% overestimation of the dark current, so dark frames matching the detector voltage of the science data are required for an accurate dark current subtraction.

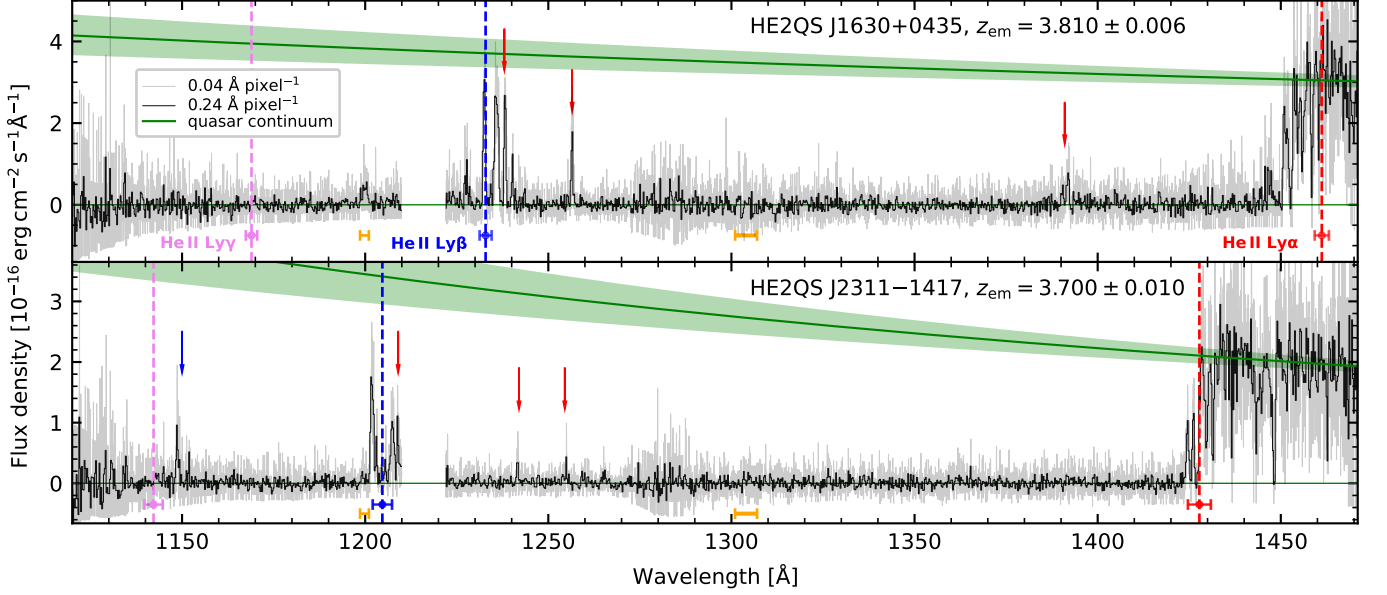


Figure 1. Extinction-corrected *HST/COS* G130M spectra of our two He II-transparent quasars sampled at $0.04 \text{ \AA pixel}^{-1}$ (2–3 pixels per resolution element, gray) and $0.24 \text{ \AA pixel}^{-1}$ (undersampled, black). The green line shows the best-fit power law continuum with 1σ error determined by W19 and corrected for quasar variability between the observation epochs. The vertical dashed lines show He II Ly α (red), Ly β (blue) and Ly γ (violet) in the quasar rest frame with indicated 1σ quasar redshift error. Visible He II Ly α and Ly β transmission spikes are marked with red and blue arrows, respectively. The spectral region contaminated by geocoronal Ly α emission at 1216 \AA is not shown. The orange horizontal lines indicate the spectral ranges around geocoronal N I $\lambda 1200$ and O I $\lambda 1304$ where we use only data taken in orbital night.

The strongest He II Ly α transmission spikes in both spectra are already known from the low-resolution data (W19), but are now resolved ($\text{FWHM} \gtrsim 50 \text{ km s}^{-1}$). Furthermore, our deep G130M data enable us to verify very weak spikes previously only tentatively detected in the G140L spectra, i.e., at $\sim 1250 \text{ \AA}$ in the HE2QS J2311–1417 spectrum (see Section 5.1). For the first time, we detect intergalactic $z > 3.4$ He II Ly β spikes at $\sim 1150 \text{ \AA}$ (HE2QS J2311–1417) and possibly at $\sim 1200 \text{ \AA}$ (HE2QS J1630+0435), which are further analyzed in Section 5.2.

The flux spikes at $\sim 1200 \text{ \AA}$ in the spectrum of HE2QS J1630+0435 lie suspiciously on top of the geocoronal N I $\lambda 1200$ line. Therefore, we closely investigated the accuracy of the geocoronal decontamination. Figure 2 shows the night-only and day-only spectra for both quasars at geocoronal O I $\lambda 1304$ and N I $\lambda 1200$. The O I $\lambda 1304$ lines show no residual flux above the detection limit at $1301 \text{ \AA}–1307 \text{ \AA}$ in both night-only spectra. However, the weaker N I $\lambda 1200$ line still seems to be present in the night-only spectrum of HE2QS J1630+0435 which is very unusual (W19). In contrast, geocoronal N I in the spectrum of HE2QS J2311–1417 vanishes as expected, while the strong spike in the He II Ly β proximity zone next to it does not change. Analysis of blank-sky *HST/COS* observations (Appendix C) could not definitely determine the origin of the flux at 1200 \AA in the HE2QS J1630+0435 spectrum. Therefore, we decided to exclude it from further analysis.

3.3. Comparison with the *HST/COS* G140L Spectra

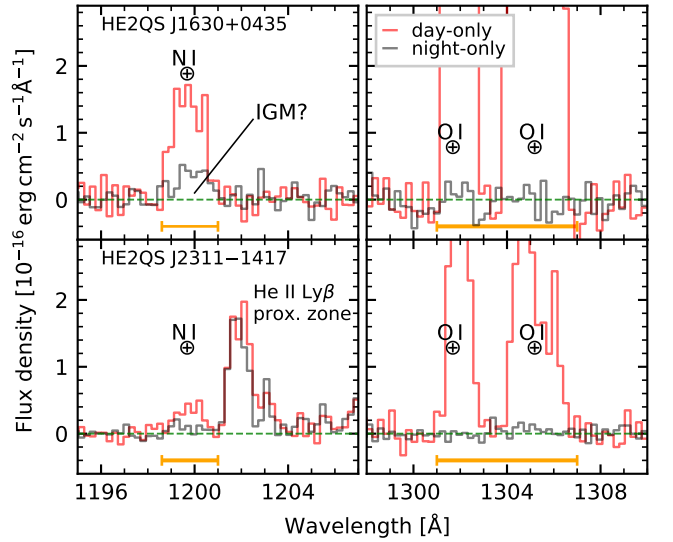


Figure 2. Comparison between day-only (red) and night-only (gray) data in spectral regions contaminated by geocoronal N I and O I for HE2QS J1630+0435 (upper panels) and HE2QS J2311–1417 (lower panels). The horizontal lines indicate spectral ranges replaced by night-only data.

We compared the G130M spectra to the low-resolution G140L data analyzed by W19. The most significant differences in the data reduction are that G140L spectra must be corrected for scattered geocoronal Ly α emission unlike our G130M data (Section 2), and that W19 neglected flat-

fielding, which is inconsequential in the wavelength range of interest.

Figures 3 and 4 show the normalized G130M and G140L He II Ly α transmission spectra using the same binning of $0.24 \text{ \AA pixel}^{-1}$. The strongest spikes previously detected in the G140L spectra are confirmed in the G130M spectra, e.g. at $z \sim 3.08$ and $z \sim 3.135$ in Figure 3. Due to the higher effective spectral resolution of the undersampled G130M data, the spikes are more prominent than in the G140L data, e.g. the spike at $z \simeq 3.135$ in Figure 3. In order to quantify the significance of the measured He II Ly α transmission, we calculated for each pixel the probability

$$P(> N|B) = 1 - \sum_{k=0}^N \frac{B^k e^{-B}}{k!} \quad (1)$$

that the detected N Poisson counts are consistent with the estimated background B . Very low P values indicate statistically significant He II transmission ($N \gg B$). In Figures 3 and 4 we have marked pixels with $P(> N|B) < 0.0227$ that correspond to a $> 2\sigma$ detection.

From the total 860 0.24 \AA pixels at $3.06 \leq z \leq 3.74$ in the spectrum of HE2QS J1630+0435 we would expect ~ 20 random pixels with $P(> N|B) < 0.0227$ from the Poisson noise alone. Therefore, we regard individual pixels as not reliable to find real transmission. Nevertheless, two or more consecutive pixels with $P(> N|B) < 0.0227$ are a good indicator for real transmission spikes, because the probability to find two such pixels arising just from Poisson noise is only $\sim 0.07\%$. Due to the varying exposure time and Poisson noise, some regions show apparent transmission, e.g. at $z = 3.20\text{--}3.24$ in the G130M data (Section 3.1). The G130M data show that some of the apparent unresolved spikes in the G140L data are caused by background Poisson noise, e.g. $z \sim 3.60$ in Figure 4). Another advantage of the G130M data, besides the higher resolution, is the fact that the contamination from scattered geocoronal Ly α emission is negligible. This is especially noticeable in the regions close to geocoronal Ly α where the G140L spectra show systematically higher transmission due to residual scattered light, i.e. at $z < 3.10$ in Figure 4.

Additionally, we measured the Ly α effective optical depth $\tau_{\text{eff}} = -\ln\langle f_{\lambda}/E_{\lambda} \rangle$, where f_{λ} is the quasar flux density corrected for Galactic extinction, E_{λ} is the respective extrapolated continuum, and $\langle \rangle$ denotes the average taken over a redshift range Δz . For comparison we adopted the same technique and the same redshift intervals $\Delta z = 0.04$ as W19. In short, we maximized the Poisson likelihood function

$$L = \prod_{j=1}^n \frac{(S_j + B_j)^{N_j} e^{-(S_j + B_j)}}{N_j!} \quad (2)$$

for n contiguous pixels in the $\Delta z = 0.04$ bin with N_j registered counts, the background B_j and the not yet determined non-integer source counts $S_j = t_j C_j K_{\text{FF},j} E_j e^{-\tau_{\text{eff}}}$ with the pixel exposure time t_j , the extinction-corrected flux calibration curve C_j , the flat-field correction $K_{\text{FF},j}$ and the continuum E_j . Figure 5 shows the measured τ_{eff} in the G130M and

G140L spectra with 2σ error bars and 2σ lower limits⁴ in case $P \geq 0.0277$ in the $\Delta z = 0.04$ bin. Except for the bin $3.06 < z < 3.10$ where the G140L data are affected by residual scattered geocoronal Ly α emission, the measurements in high-resolution and low-resolution data are in very close agreement. The G130M data have a comparable or higher sensitivity to high τ_{eff} values than the G140L data.

In summary, the G130M data are overall more reliable than the G140L data according to the τ_{eff} measurements. Furthermore, their higher resolution enables us to detect narrow transmission spikes at high significance to distinguish them from Poisson noise.

4. HE II TRANSMISSION SPIKES IN REALISTIC MOCK SPECTRA

4.1. He II Mock Spectra from a Hydrodynamical Simulation

4.1.1. Simulation and UV Background Models

To constrain the He II reionization history with He II transmission spikes we must compare our data to realistic mock spectra from a numerical simulation with a given He II photoionization rate $\Gamma_{\text{He II}}$, or equivalently with a given He II fraction $x_{\text{He II}}$. We used $\Delta z = 0.04$ long skewers from W19, which had been created from outputs of a cubic (146 cMpc)³ hydrodynamical simulation performed with the N_{YX} code (Almgren et al. 2013; Lukić et al. 2015) applying photoionization and photoheating rates from Haardt & Madau (2012). The skewers had been made for the W19 effective optical depth measurements on a length scale $\Delta z = 0.04$ (34 cMpc at $z = 3.5$) in the redshift range $2.56 \leq z \leq 3.88$, and were initially longer ($\Delta z = 0.08$) to account for the low-resolution G140L line spread function (W19). At each redshift we used only the central $\Delta z = 0.04$ of the available 1000 skewers with a pixel size of $2\text{--}3 \text{ km s}^{-1}$. The He II Ly α optical depths were rescaled according to the UV background models as $\tau_{\alpha} \propto \Gamma_{\text{He II}}^{-1}$ in the optically thin limit, which approximately holds at the tail end of the He II reionization epoch.

We infer photoionization rates from our observed data by using the predictions from a set of spatially uniform UV background models with different amplitudes. We created 1000 synthetic spectra for He II Ly α and He II Ly β separately for a set of constant photoionization rates ($10^{-16.4} \text{ s}^{-1} \leq \Gamma_{\text{He II}} \leq 10^{-13.3} \text{ s}^{-1}$ with step size $\Delta[\log(\Gamma_{\text{He II}}/\text{s}^{-1})] = 0.1$) by concatenating the $\Delta z = 0.04$ skewers. Additionally, we used a spatially fluctuating UV background model (Davies et al. 2017) for comparison, and to model foreground $z_{\text{fg}} < 3$ He II Ly α absorption that overlaps with the high-redshift Ly β absorption (Fig. 1). This model was calculated in a (500 cMpc)³ volume with grid cells of (7.8 cMpc)³ using an analytic IGM absorber model and a quasar luminosity function, resulting in a spatially varying mean free path that increases from $\sim 20 \text{ cMpc}$ at $z = 3.2$ to $\sim 40 \text{ cMpc}$ at $z = 2.8$. The usage of this specific model is justified by its excellent reproduction of the observed large-scale variations in the

⁴ W19 used 1σ errors and lower limits.

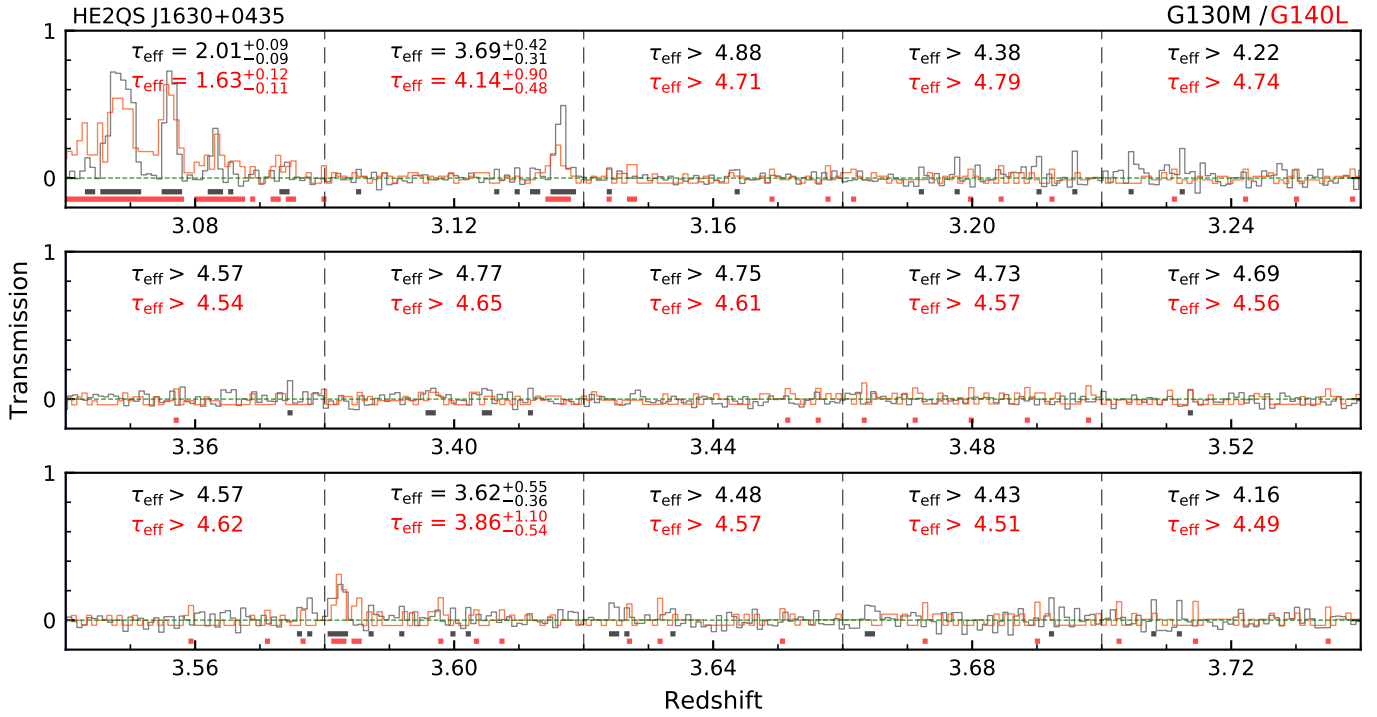


Figure 3. High-resolution G130M (gray) and low-resolution G140L (red, W19) Ly α transmission spectra of HE2QS J1630+0435 binned to $0.24 \text{ \AA pixel}^{-1}$. The thick red and black points and lines underneath the zero line (dotted line) indicate pixels with Poisson probability $P(> N|B) < 0.0227$, i.e. pixels with transmission detected at $> 2\sigma$ significance. We also indicate the effective optical depths measured in $\Delta z = 0.04$ intervals (vertical lines) with 2σ double-sided Poisson error bars, or as 2σ lower limits if $P(> N|B) \geq 0.0227$.

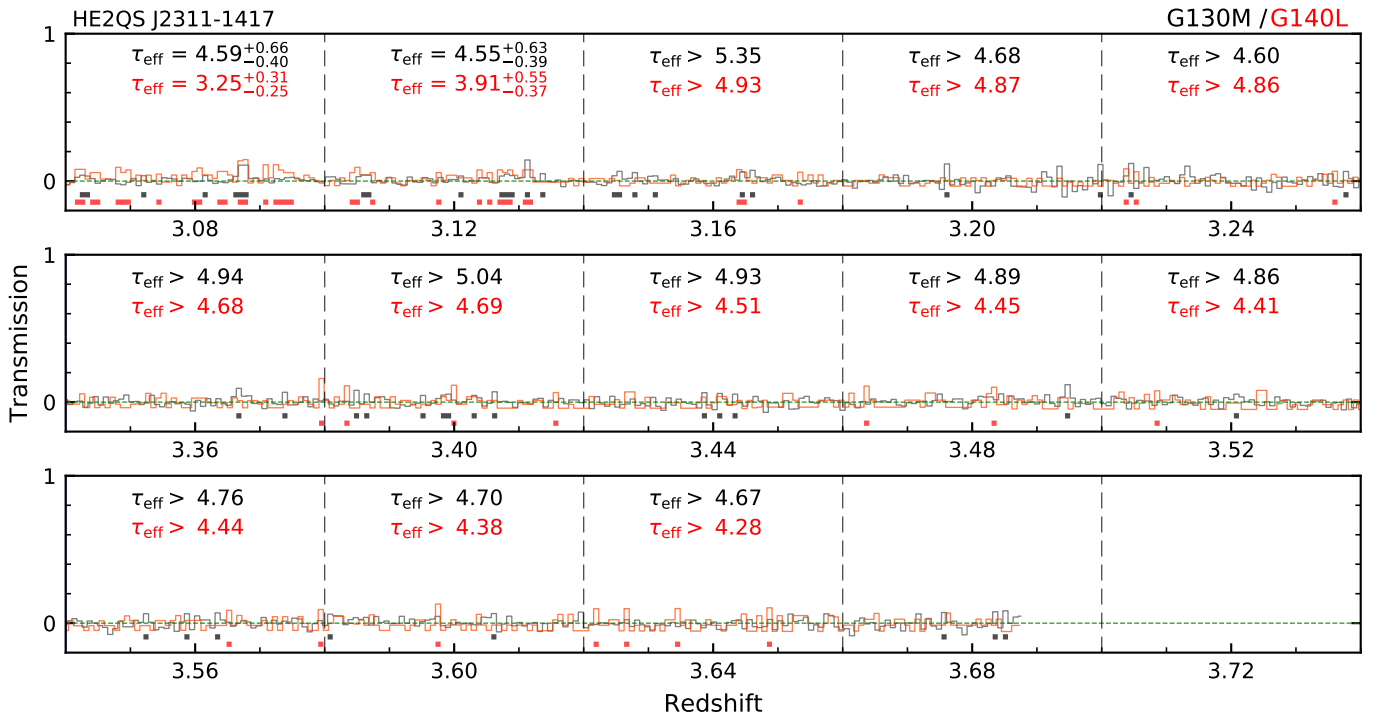


Figure 4. Similar to Figure 3 but for HE2QS J2311–1417.

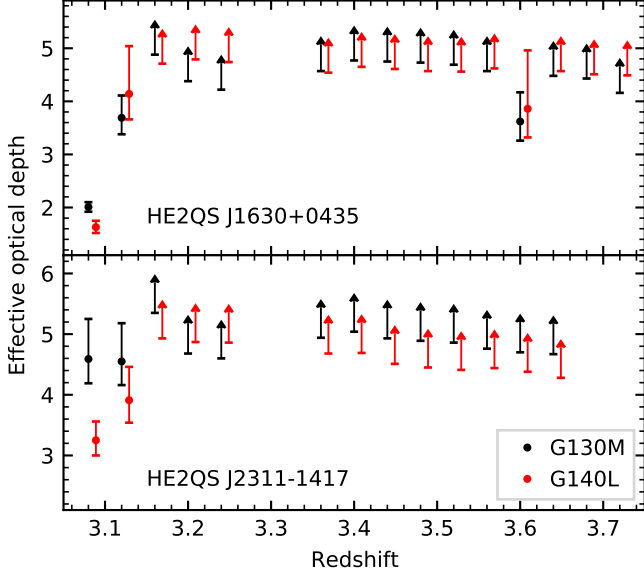


Figure 5. Comparison of the He II Ly α effective optical depths measured in G140L (red) and G130M (black) spectra with double-sided 2σ Poisson errors or 2σ lower limits (arrows). The redshift range $3.26 < z < 3.34$ is not reliable due to possible residual geocoronal O I contamination in the G140L data.

$z < 3.3$ He II Ly α effective optical depths (W19). Applying it to the outputs of the $(146 \text{ cMpc})^3$ hydrodynamical simulation, we sufficiently capture He II transmission features sourced by the density field and by UV background fluctuations. By doing so, we lose the correlation between the density field and radiation field, however, due to the rarity of quasars and long mean free path the correlation is expected to be fairly weak.

4.1.2. Mock Spectra for He II Ly α

First, for any given He II photoionization rate, random synthetic spectra were concatenated to 1000 long He II Ly α transmission spectra covering the common redshift range $3.06 \leq z_\alpha \leq 3.66$. The redshift ranges covered by only one of the sightlines are too short for the analysis. The concatenation does not affect the final statistical comparison of the transmission spikes in smaller redshift bins $\Delta z = 0.15$ that account for possible redshift evolution of the He II photoionization rate. Density discontinuities at the edges of the concatenated skewers are not of a concern due to the strong absorption. We excluded skewers with H I Ly α optical depths $\tau_{\text{HI}} > 3000$ that correspond to H I column densities $N_{\text{HI}} \geq 10^{17.1} \text{ cm}^{-2}$, because a lack of strong H I Lyman limit systems is required to render He II observable.

Realistic COS mock spectra matching the characteristics of the observed spectra were produced as in W19. First, we applied the *HST*/COS G130M line-spread function to the synthetic He II Ly α transmission spectra. We used the exposure time weighted average *HST*/COS line-spread function at 1300 \AA corresponding to $R \sim 14,000$, which is sufficient at our low Poisson $S/N \lesssim 3$. Then, the synthetic spectra

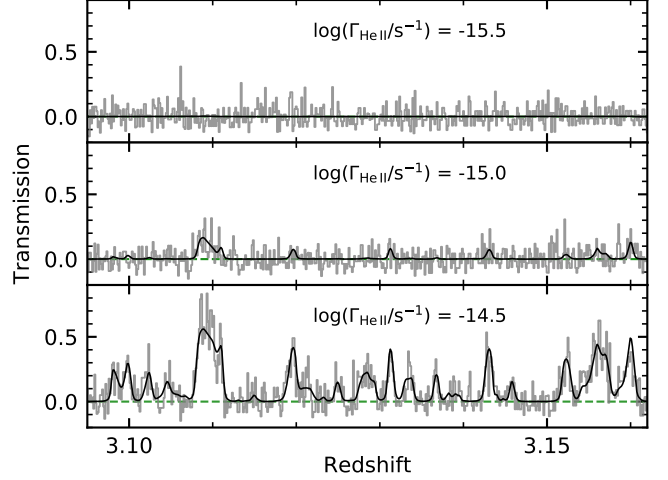


Figure 6. The effect of the photoionization rate on the number of spikes in He II Ly α mock spectra. The panels show the simulated He II transmission at G130M resolution with (gray) and without (black) Poisson noise for the same skewer.

were rebinned to the wavelength grid of the observed spectra. Next, we used the calibration curve, the pixel exposure time and the background model of the observed spectra to convert the He II transmission to expected counts. Finally, the COS counts were simulated by adding Poisson noise according to the expected counts per pixel. To incorporate the estimated systematic background subtraction error, the background model of the observed spectra was varied assuming a Gaussian distribution with a standard deviation according to the estimated systematic error.

Figure 6 shows the effect of the photoionization rate on the He II Ly α transmission in mock spectra of the same density skewer. Generally, He II transmission features arise in IGM underdensities (Croft et al. 1997). A higher photoionization rate results in stronger and more numerous spiky features from the emerging He II Ly α forest. It also shows that the smallest features disappear in the noise as in the observed spectra.

4.1.3. Mock Spectra for He II Ly β

The He II Ly β forest overlaps with foreground He II Ly α absorption at $z_{\text{fg}} = (1 + z_\beta)\lambda_\beta/\lambda_\alpha - 1$. Pure He II Ly β skewers were created by rescaling the optical depths of the He II Ly α skewers by the respective rest frame wavelengths and oscillator strengths as

$$\tau_\beta(z_\beta) = \frac{\lambda_\beta f_\beta}{\lambda_\alpha f_\alpha} \tau_\alpha(z_\beta) \approx 0.160 \tau_\alpha(z_\beta) \quad . \quad (3)$$

Similarly to the He II Ly α spectra, we concatenated random skewers to match the IGM He II Ly β regions of the observed spectra ($3.46 \leq z_\beta \leq 3.685$ for HE2QS J2311-1417 and $3.56 \leq z_\beta \leq 3.72$ for HE2QS J1630+0435). Then we added foreground Ly α absorption from random $N_{\text{Ly}\alpha}$ skewers using the fluctuating UV background model by Davies et al. (2017), resulting in a total optical depth $\tau(z_\beta) = \tau_\beta(z_\beta) +$

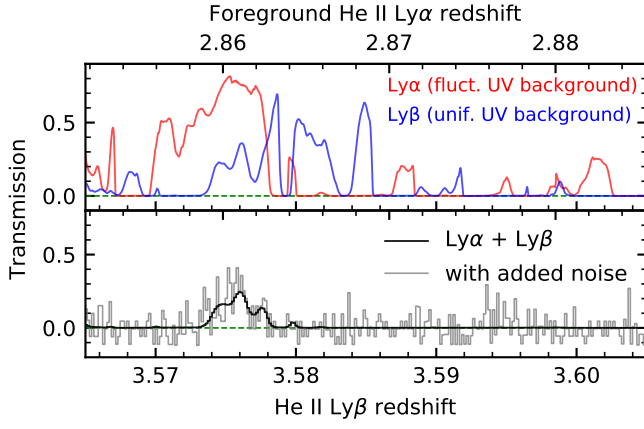


Figure 7. Creation of He II Ly β mock spectra. *Upper panel:* Two random $\Delta z = 0.08$ He II transmission skewers for high-redshift Ly β ($z_\beta \sim 3.58$, blue) and low-redshift Ly α ($z_{fg} \sim 2.87$, red). *Lower panel:* Overlapped, i.e. multiplied He II Ly α and Ly β transmission with (gray) and without (black) Poisson noise.

$\tau_\alpha(z_{fg})$. Figure 7 illustrates our procedure for the equivalent multiplication of the transmission spectra. The remaining steps are identical to the creation of the He II Ly α mock spectra.

4.2. Automated Measurement of Transmission Spikes

We developed a fully automated code that detects and fits all significant transmission features with multiple Gaussian profiles. An automated routine is crucial for our analysis, because it provides consistent and reproducible results for the observed and the fully forward-modeled mock He II absorption spectra, respectively. Due to the strong He II absorption we model multiplicative transmission features with additive Gaussian profiles, similar to procedures to model $z \gtrsim 5.5$ H I transmission spikes (Barnett et al. 2017; Chardin et al. 2018; Gaikwad et al. 2020; Yang et al. 2020). While such decompositions are entirely empirical, the statistical properties of the detected transmission spikes, such as their incidence and their equivalent widths, can be used to constrain the ionization state of the IGM. Henceforth, our primary statistic of interest is the incidence of transmission spikes, i.e. the number of Gaussian components in predefined redshift bins.

In order to locate and fit transmission spikes, we must define spectral regions that are long enough to reliably fit a Gaussian profile while limiting the impact of Poisson noise. First, we calculated the probability P (Equation 1) as a 0.36 \AA (9-pixel) running average to reduce the Poisson noise of individual pixels in finding significant transmission. Then, we considered regions with $n \geq 9$ consecutive pixels with detected transmission at $> 3\sigma$ significance (running average $P < 0.0014$) for a fit of Gaussian profiles. Our choice of ≥ 9 pixels (3–4 resolution elements) is a good compromise between the resolving power and the quality ($S/N \lesssim 3$) of our data. The very conservative probability limit $P < 0.0014$ ensures that most of the spikes induced by Poisson noise will

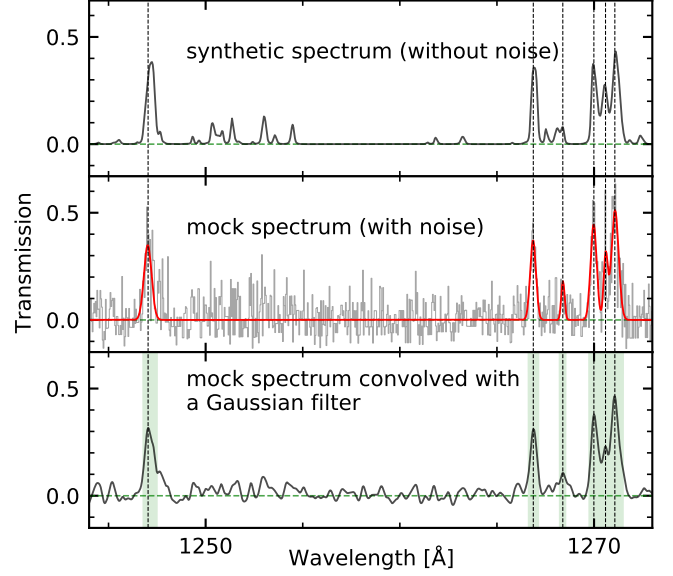


Figure 8. Detected transmission spikes in a He II Ly α mock spectrum. *Upper panel:* Synthetic spectrum without noise. *Middle panel:* Mock spectrum with Poisson noise (gray) with best-fit Gaussian components (red). *Lower panel:* Noisy mock spectrum convolved with the Gaussian filter with $\sigma_f = 0.1 \text{ \AA}$. Green-shaded areas indicate regions of ≥ 9 consecutive pixels ($\geq 0.36 \text{ \AA}$) where the 9-pixel running average of P (Equation 1) is < 0.0014 . The vertical lines indicate the positions of the peak centers found by the Python routine `scipy.signal.find_peaks()` in the green-shaded areas.

be excluded from the analysis at the expense of the weakest spikes at the resolution limit of the data.

In order to find the positions λ_m of multiple spikes in the considered spectral region, we used the Python routine `scipy.signal.find_peaks()` after smoothing the spectra with a Gaussian filter $\sigma_f = 0.1 \text{ \AA}$. With the resulting number of components M and their individual positions λ_m , we fitted their heights A_m and widths (Gaussian standard deviation σ_m) by maximizing the Poisson likelihood function (Equation 2) in the $n \geq 9$ pixel wide region. The He II transmission was modeled as the sum of the M Gaussian components, such that the modeled counts per pixel in Equation 2 becomes

$$S_j = t_j C_j K_{FF,j} E_j \sum_{m=1}^M A_m e^{-(\lambda_m - \lambda_j)^2 / (2\sigma_m^2)} \quad . \quad (4)$$

Because our fit parameters are not physical but empirical, we refrained from computing their statistical errors.

Figure 8 illustrates the spike finding process for a representative He II Ly α mock spectrum. The comparison between the noise-free spectrum (upper panel) and the Gaussian decomposition of the mock spectrum (middle panel) shows that the strong transmission peaks are found reliably. In the mock spectra $> 99\%$ (50%) of the spikes with $A_m \geq 0.25$ ($A_m = 0.12$) are recovered. Small spikes, e.g. at $\lambda \sim 1252 \text{ \AA}$ in Figure 8, are often lost in the noise as expected. Others, e.g. at $\lambda \sim 1268 \text{ \AA}$, cannot be fitted as precisely as stronger

Table 3. Fitting parameters of the He II Ly α transmission spikes.

Object	$z_{\alpha,m}$	σ_m	A_m
		[km s $^{-1}$]	
HE2QS J1630+0435	3.0636	321	0.086
	3.0675	41	0.777
	3.0691	92	0.660
	3.0762	62	0.794
	3.0829	45	0.322
	3.1365	40	0.593
	3.5812	22	0.231
	3.5825	35	0.280
HE2QS J2311–1417	2.9688	45	0.120
	2.9747	120	0.308
	2.9794	43	0.374
	2.9818	53	0.123
	3.0875	36	0.157
	3.1314	24	0.189
	3.1662	29	0.080

spikes. On average, the algorithm slightly overestimates the spike heights due to the asymmetric Poisson noise. The recovery rate mainly varies with the height of the spikes but not with their width. In the end, the recovery rate and the fitting accuracy are not particularly relevant, because the same algorithm is applied to the observed spectra and to the forward-modeled mock spectra alike.

5. RESULTS

5.1. Fitted Observed He II Ly α Transmission Spikes

Figure 9 displays the spectral regions in the two sightlines that show statistically significant IGM He II Ly α transmission spikes. Most transmission spikes are detected in the narrow redshift range $3.06 \lesssim z_{\alpha} \lesssim 3.17$ (~ 100 cMpc) in both lines of sight. Their clustered appearance suggests that He II at $z \sim 3.1$ is highly ionized in both sightlines. At higher redshifts we measure two blended spikes at $z_{\alpha} \approx 3.58$ in the HE2QS J1630+0435 spectrum. Some of the transmission spikes might arise from transverse proximity effects of foreground quasars (e.g., Jakobsen et al. 2003; Schmidt et al. 2017), but the largest dedicated survey to date (Schmidt et al. 2017) did not cover HE2QS J2311–1417, while HE2QS J1630+0435 requires deeper imaging and follow-up spectroscopy to find matching $z_{\text{em}} > 3$ quasars. In general, the degeneracies imposed by quasar lifetime and obscuration require a statistical analysis (Schmidt et al. 2017, 2018). In the HE2QS J2311–1417 sightline, the four spikes at $z_{\alpha} = 2.97$ – 2.98 are likely IGM Ly α spikes rather than Ly β spikes of the proximity zone (Figure 1), because of the lack of correlation with the Ly α proximity zone. However, due to the small additional pathlength ($\Delta z_{\alpha} = 0.017$) between He II Ly β and geocoronal Ly α we excluded this region from the statistical analysis in Section 5.3.

Table 4. Fitting parameters of the He II Ly β transmission spikes.

Object	$z_{\beta,m}$	σ_m	A_m
		[km s $^{-1}$]	
HE2QS J2311–1417	3.4817	54	0.252
	3.4840	16	0.220
	3.4945	28	0.146

Between these isolated Ly α transmission features both spectra display long Gunn-Peterson troughs without significant transmission. The troughs are at $3.138 \leq z_{\alpha} \leq 3.580$ (383 cMpc) in the HE2QS J1630+0435 spectrum, and at $3.167 \leq z_{\alpha} \leq 3.685$ (443 cMpc) in the HE2QS J2311–1417 spectrum, with 2σ detection limits of $\tau_{\text{eff}} > 5.82$ and $\tau_{\text{eff}} > 6.13$, respectively.

Table 3 lists the fitting parameters of the He II Ly α transmission spikes as individual Gaussian components. The combined transmission of the Gaussians at $z_{\alpha} \approx 3.065$ in the spectrum of HE2QS J1630+0435 appears unphysical, because it exceeds unity. However, because our method is entirely empirical, we chose not to limit the total transmission. Such effects also appear in the mock spectra and they do not affect our results. Likewise, we did not include continuum uncertainty, because it does not change the incidence of the spikes.

5.2. Fitted Observed He II Ly β Transmission Spikes

The HE2QS J2311–1417 spectrum contains three significant He II Ly β transmission spikes at $z_{\beta} \sim 3.49$, presented in Figure 10 and tabulated in Table 4. The strongest of these was already foreshadowed by a single high-transmission pixel in the G140L spectrum, which is as unreliable as most individual Ly α transmission pixels (Figures 3 and 4). Here we confirm this suggestion with superior data. This is the first time that significant He II Ly β transmission is detected and resolved at $z_{\beta} > 3.4$, suggesting the presence of highly ionized patches in the $z > 3.4$ IGM that are saturated in He II Ly α at He II fractions of a few percent (McQuinn 2009). Previous studies considered lower redshifts, and focused on the He II Ly β effective optical depth to reach higher sensitivity in He II Ly α (Zheng et al. 2004; Syphers et al. 2011). The results were plagued by low data quality and systematics due to the required modeling of He II Ly α foreground absorption (Syphers et al. 2011). Here, we capitalize on spectral resolution, data quality, redshift coverage and detailed mock spectra to better constrain the ionization state of the IGM. Finally, while there are hints that also the HE2QS J1630+0435 sightline shows IGM He II Ly β transmission (Appendix C), we cannot definitely prove its origin, so we exclude it from further analysis (see Appendix D for the alternative assertion).

We emphasize that both sightlines had been selected for observation solely because of their FUV brightness and thus,

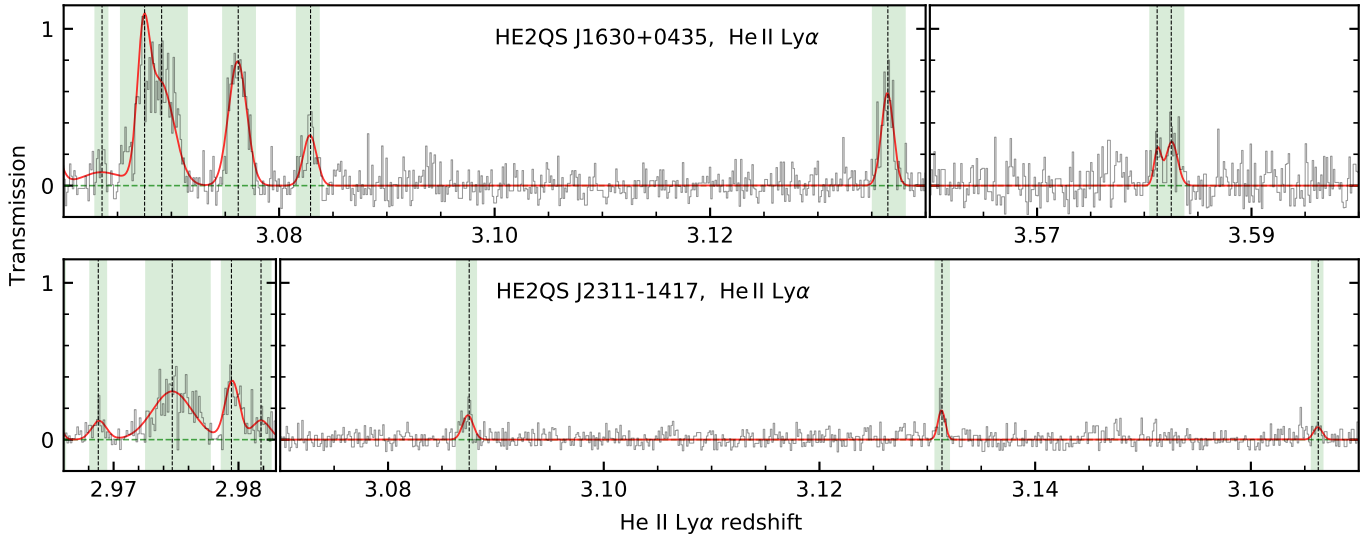


Figure 9. Regions with detected $\text{Ly}\alpha$ transmission spikes in the *HST*/COS G130M spectra of both sightlines (gray). The green-shaded areas indicate regions with $n \geq 9$ consecutive pixels with significant transmission ($P \leq 0.0014$, Equation 1). Detected peaks (spike locations) are marked with vertical lines. Red curves show the Gaussian decompositions of the sometimes blended transmission features.

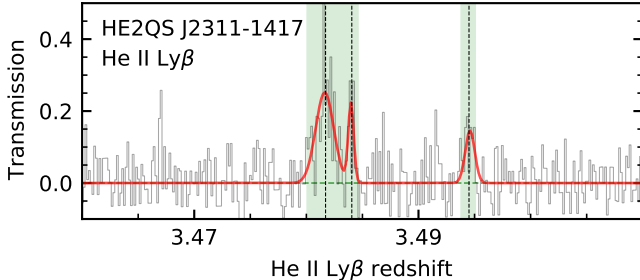


Figure 10. Similar to Figure 9 but for He II $\text{Ly}\beta$.

our very modest sample is unbiased with respect to the spike incidence. Thus, the very fact that we detect He II $\text{Ly}\beta$ transmission at $z_\beta \approx 3.49$ in the HE2QS J2311–1417 sightline despite foreground contamination, together with definite $\text{Ly}\alpha$ transmission at $z_\alpha \approx 3.58$ and possible $\text{Ly}\beta$ transmission at $z_\beta \approx 3.68$ toward HE2QS J1630+0435, supports suggestions of patchy He II reionization (i.e. a fluctuating UV background) at $z > 3.4$ (W19).

5.3. Implications for the He II Photoionization Rate

Evidently, a higher He II photoionization rate increases the number and amplitude of He II $\text{Ly}\alpha$ transmission features (Figure 6). In order to study this dependence in more quantitative terms, we constructed complementary cumulative distribution functions (CCDFs) from the probability mass functions of the incidence of spikes in our mock spectra. The $\text{CCDF}(n)$ is the fraction of mock spectra with more than n detected spikes. For every grid point in Γ_{HeII} , we computed the CCDF of $\text{Ly}\alpha$ transmission spikes from mock spectra of both sightlines in $\Delta z = 0.15$ redshift bins. By using $\Delta z = 0.15$ bins (combined pathlength ~ 260 cMpc), we decrease the impact of density fluctuations on the measurement while tracking the redshift evolution of the photoionization

rate. The combination of the individual sightlines is justified due to their similar spike recovery rates.

Figure 11 shows the resulting CCDFs for representative photoionization rate grid values. Although each CCDF spans a wide range due to IGM density fluctuations, the CCDFs monotonically shift to higher numbers of $\text{Ly}\alpha$ spikes with increasing Γ_{HeII} . Therefore, while our spike decomposition is empirical, we are able to infer a physical parameter, the characteristic He II photoionization rate from the measured spike incidence. Thanks to our forward-modeling, the CCDFs include the instrumental effects and data quality limitations. For comparison, we also computed CCDFs for the fluctuating UV background from Davies et al. (2017) which are consistent with our measured spike incidence. For example at $z \sim 3.1$, in 40 % of the mock data there are between 5 and 13 spikes. Furthermore, the non-detection at $z = 3.2$ – 3.5 is very common since ~ 25 % of the mock data show no spikes.

In order to infer the He II photoionization rates, we have to assume that our two sightlines are representative of the IGM. We determined Γ_{HeII} from the number of detected He II $\text{Ly}\alpha$ transmission spikes in $\Delta z = 0.15$ bins. For this, we constructed posterior probability distributions $p(\Gamma_{\text{HeII}}|n_\alpha)$ for the number of detected He II $\text{Ly}\alpha$ spikes n_α (Figure 11) by using Bayes’ theorem

$$p(\Gamma_{\text{HeII}}|n_\alpha) \propto L(n_\alpha|\Gamma_{\text{HeII}})p(\Gamma_{\text{HeII}}) \quad (5)$$

with a uniform prior $p(\Gamma_{\text{HeII}})$ on a refined grid $\Delta[\log(\Gamma_{\text{HeII}}/s^{-1})] = 0.05$ to adequately sample the posterior and the likelihood $L(n_\alpha|\Gamma_{\text{HeII}})$ derived from the probability mass functions of the spike incidence. The posterior was normalized to unit integral. We quote the median value of the posterior distribution as our Γ_{HeII} measurement, and the equal-tailed 84th–16th percentile range as its 1σ uncertainty. The redshift bins without detected transmission spikes yield 1σ upper limits from the 84th percentile of the posterior.

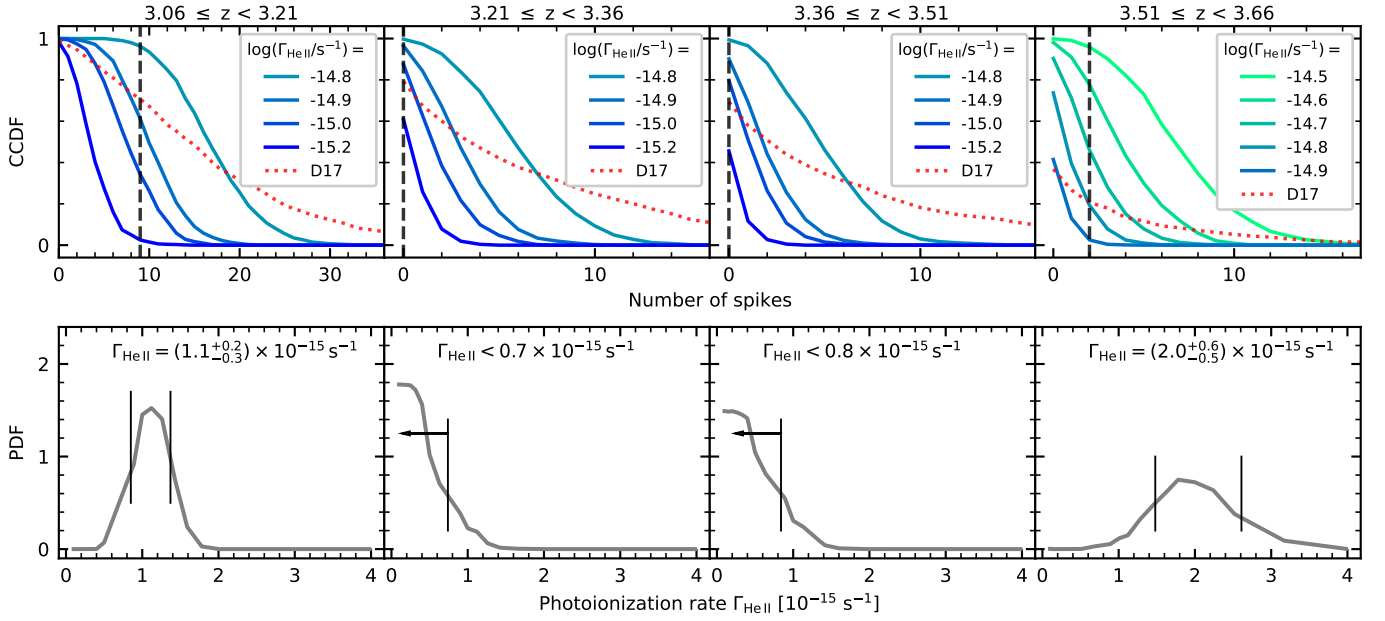


Figure 11. Top: CCDFs of the incidence of He II Ly α spikes for different uniform photoionization rates in $\Delta z = 0.15$ derived from realistic mock COS spectra for our two sightlines. Although the CCDFs are discrete, they are plotted as non-discrete distributions for illustration purposes. The vertical dashed lines show the number of detected spikes in our observed spectra in the corresponding redshift bin. The red dotted lines indicate CCDFs with the fluctuating UV background model from Davies et al. (2017) shown here for comparison. Bottom: Normalized posterior probability density functions (PDFs) of Γ_{HeII} given the measured number of spikes (Equation 5). The posterior median yields our inferred Γ_{HeII} value (labeled), with the 16th–84th percentile range (vertical lines) as 1σ uncertainty.

Table 5. Median Γ_{HeII} inferred from the number of He II Ly α or Ly β transmission spikes in redshift bins Δz .

Object	Δz	$\Gamma_{\text{HeII}} (10^{-15} \text{ s}^{-1})$	Transition
Both	3.06–3.21	$1.1^{+0.2}_{-0.3}$	Ly α
	3.21–3.36	< 0.7	Ly α
	3.36–3.51	< 0.8	Ly α
	3.51–3.66	$2.0^{+0.6}_{-0.5}$	Ly α
HE2QS J2311–1417	3.46–3.685	$1.1^{+0.9}_{-0.4}$	Ly β
HE2QS J1630+0435	3.56–3.72	0.9 ± 0.3	Ly β and Ly α
		$2.3^{+0.7}_{-0.6}$	Ly β and Ly α

We detect nine spikes at $3.06 \leq z < 3.21$ and two spikes at $3.51 \leq z < 3.66$, resulting in two measurements of the He II photoionization rate (Table 5). In the other two redshift bins we derive only upper limits due to the lack of spikes. Repeating the above analysis for the total equivalent width of the detected spikes instead of their incidence resulted in similar Γ_{HeII} values within the broad confidence intervals. Somewhat larger redshift bins ($\Delta z = 0.2$) do not significantly change our results either.

In contrast to He II Ly α , the spectral regions covering He II Ly β in both sightlines have only a short overlap of $\Delta z \sim 0.12$. Thus, we analyzed the sightlines independently (Figure 12). Similar to He II Ly α , the fluctuating UV background model (Davies et al. 2017) is consistent with the measured He II Ly β

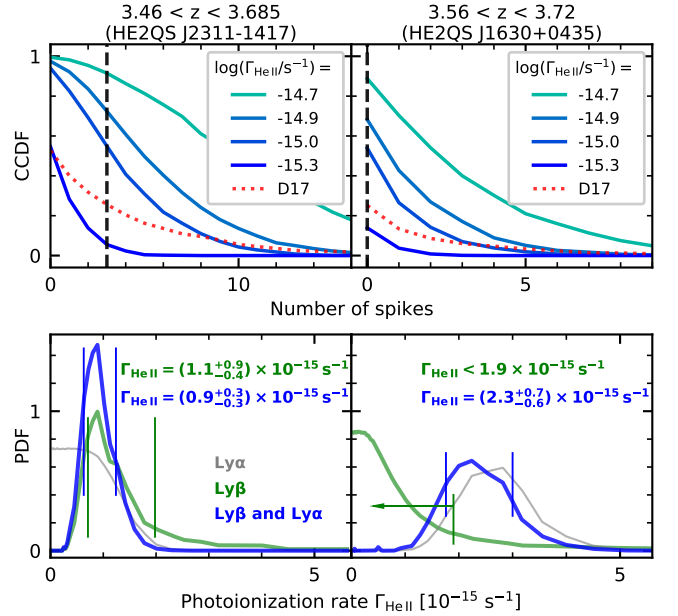


Figure 12. Similar to Figure 11 but for He II Ly β and separately for each sightline. The bottom panel shows the PDFs inferred from Ly α (gray), Ly β (green) and from both transitions combined (blue).

spike incidence, e.g. in 35% of sightlines at $z = 3.46$ – 3.685 there are between 1 and 5 spikes. The posteriors inferred just from the detected He II Ly β spikes n_{β} are highly asymmet-

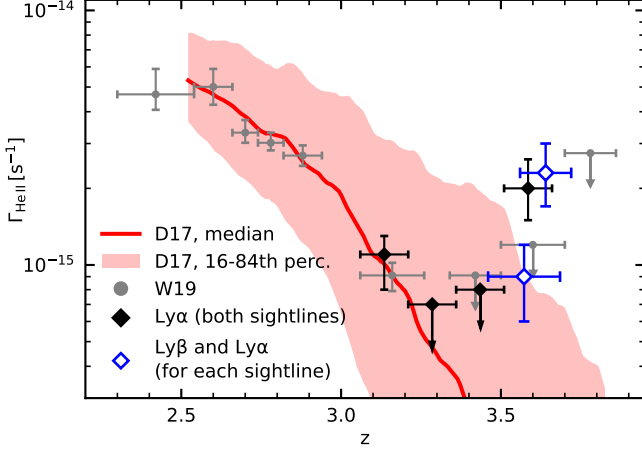


Figure 13. Redshift evolution of the He II photoionization rate inferred from the incidence of transmission spikes (diamonds) and from the effective optical depth (circles, W19). Error bars show the 16th–84th percentile range derived from the Γ_{HeII} posterior given the measured number of spikes. Upper limits are inferred from 84th percentile of the Γ_{HeII} posterior. The red curve shows the median $\Gamma_{\text{HeII}}(z)$ and its 16th–84th percentile range (red-shaded) from 3D semianalytic calculations (Davies et al. 2017).

ric and wider in comparison to those of He II Ly α , mostly due to the required He II Ly α foreground modeling using the fluctuating UV background. Since the Ly β redshift range of each sightline has simultaneous Ly α coverage we used a joint likelihood for detecting n_α and n_β spikes to construct the combined posterior

$$p(\Gamma_{\text{HeII}}|n_\alpha, n_\beta) \propto L(n_\alpha|\Gamma_{\text{HeII}})L(n_\beta|\Gamma_{\text{HeII}})p(\Gamma_{\text{HeII}}) \quad (6)$$

The spike incidences n_α and n_β can be considered independent due to the overlapping foreground He II Ly α absorption. By using the combined posterior we obtain a more precise Γ_{HeII} constraint toward HE2QS J2311–1417 ($\Gamma_{\text{HeII}} = (0.9 \pm 0.3) \times 10^{-15} \text{ s}^{-1}$ for $n_\alpha = 0$ and $n_\beta = 3$ at $z = 3.46\text{--}3.685$) and an actual measurement toward HE2QS J1630+0435 instead of the upper limit ($\Gamma_{\text{HeII}} = (2.3^{+0.7}_{-0.6}) \times 10^{-15} \text{ s}^{-1}$ for $n_\alpha = 2$ and $n_\beta = 0$ at $z = 3.56\text{--}3.72$). The values are consistent with those obtained from Ly α at 2σ (Table 5).

The measured Γ_{HeII} values are plotted in Figure 13 along with the results from W19 and the prediction from the fluctuating UV background model by Davies et al. (2017). At $z < 3.5$, our new measurements are consistent with the model and Γ_{HeII} derived from τ_{eff} measurements (W19). At $z > 3.5$ the measurements are higher than expected because of the detected He II Ly α and Ly β spikes along both lines of sight. Nevertheless, they are roughly consistent with the expected Γ_{HeII} fluctuations in the Davies et al. (2017) model. This consistency is further supported with the D17 CCDFs shown in Figures 11 and 12. A measurement of a representative median Γ_{HeII} for the IGM as a whole requires a substantially larger sample.

6. SUMMARY

We have presented and analyzed new high-resolution ($R \sim 14,000$) *HST/COS* spectra of the two UV-brightest He II-transparent quasars at $z_{\text{em}} > 3.5$ (Figure 1). The high resolution and data quality ($S/N \sim 3$ per 0.04 \AA pixel) for the first time enables us to study narrow resolved ($\text{FWHM} \gtrsim 50 \text{ km s}^{-1}$) He II transmission spikes at $z > 3.4$ originating in highly ionized underdense regions in the IGM. We have analyzed the incidence of He II Ly α and Ly β transmission spikes in both spectra, using a new fully automatic routine for our Poisson-limited data that enables a one-to-one comparison to forward-modeled spectra from numerical simulations. Our main results are the following:

1. We confirm the most prominent $z > 3.06$ Ly α spikes from previous low-resolution data (W19) and measure their properties (Figure 9). The vast majority of the He II Ly α spikes (13/15) reside at $z < 3.2$, indicating mostly ionized intergalactic helium in both sightlines at these redshifts, in agreement with the τ_{eff} measurements from the larger low-resolution sample (W19). However in one sightline (HE2QS J1630+0435), two He II Ly α spikes at $z \approx 3.58$ adjacent to a $\sim 383 \text{ cMpc}$ Gunn-Peterson trough suggest the occasional presence of highly ionized underdense IGM regions also at higher redshifts.
2. We report the first detection of a group of three resolved He II Ly β transmission spikes at $z \sim 3.49$ toward HE2QS J2311–1417, where He II Ly α is fully saturated. This further supports our inferences from He II Ly α transmission in the other sightline at similar redshifts.
3. We inferred the IGM He II photoionization rates at $3.1 \lesssim z \lesssim 3.6$ by comparing our measured spike incidence to predictions from forward-modeled mock spectra from a $(146 \text{ cMpc})^3$ hydrodynamical simulation. Despite the limitation of our small sample and our assumption of a spatially uniform UV background, our inferred $\Gamma_{\text{HeII}} \sim 10^{-15} \text{ s}^{-1}$ at $z \approx 3.1$ is comparable to previous measurements and models. At higher redshifts, the transmission spikes detected in both sightlines result in higher Γ_{HeII} . However, although these values may not be representative of the average Γ_{HeII} in the IGM, they suggest a fluctuating UV background at the end of the He II reionization epoch (Davies et al. 2017).

This is the first time that small-scale structure in high-redshift He II absorption has been detected and consistently analyzed, similarly to H I studies at $z > 5.5$ (Chardin et al. 2018; Garaldi et al. 2019b; Gaikwad et al. 2020; Yang et al. 2020). We conclude that He II Ly α and Ly β transmission spike statistics are promising tools to probe the tail end of the He II reionization epoch. Further progress will require improved large-volume high-resolution hydrodynamical simulations capable of resolving underdense voids that dominate the He II absorption. While including full radiative

transfer in these simulations may still be infeasible, approximate methods successfully capture the large-scale fluctuations of the He II-ionizing background that give rise to the observed transmission spikes (Davies et al. 2017). Observationally, our very modest sample of two $z > 3.5$ sightlines may be increased by high-resolution *HST*/COS follow-up of recently discovered FUV-bright quasars (e.g., *HST* program 16317, PI Worseck). However, at $z \gtrsim 3.2$ where a study of patchy He II absorption is worthwhile, there are currently less than ten quasars bright enough for a high-resolution *HST* spectroscopy, four of which have been observed until now. Moreover, with our simulations and the Davies et al. (2017) model we predict that $\sim 30\%$ of the He II Ly α transmission spikes have FWHM = 10–20 km s $^{-1}$. These will be securely detected and resolved only with FUV-sensitive spectrographs onboard future large space telescopes (e.g., LUVOIR-A/LUMOS, The LUVOIR Team 2019) that will gather routinely $R \sim 30,000$ spectroscopy of more abundant faint (FUV ~ 23) He II-transparent quasars.

ACKNOWLEDGMENTS

We thank the anonymous referee for very helpful comments. This work was funded by Bundesministerium für Wirtschaft und Energie in the framework of the Verbundforschung of the Deutsches Zentrum für Luft- und Raumfahrt (DLR, grant 50 OR 1813). Support for program GO 15356 was provided by NASA through a grant from the Space Telescope Science Institute, which is operated by the Association of Universities for Research in Astronomy, Inc., under NASA contract NAS5-26555.

This research made use of Astropy, a community-developed core Python package for Astronomy (Astropy Collaboration et al. 2013, 2018).

Facility: *HST* (COS)

Software: astropy (Astropy Collaboration et al. 2013, 2018), SciPy (Virtanen et al. 2020), numpy (van der Walt et al. 2011), matplotlib (Hunter 2007)

APPENDIX

A. FAINTCOS – AN IMPROVED *HST*/COS REDUCTION PIPELINE FOR FAINT OBJECTS

It is known that the standard *HST*/COS reduction pipeline CALCOS miscalculates the COS FUV detector dark current due to the inhomogeneously degrading detector sensitivity (Syphers et al. 2012; Worseck et al. 2016). Because the accurate estimation of the background is essential for the analysis *HST*/COS spectra of faint objects ($f_{\lambda} \lesssim 10^{-16}$ erg cm $^{-2}$ s $^{-1}$ Å $^{-1}$), we developed an improved reduction pipeline FaintCOS, a publicly available Python code for a fast and science-grade reduction of COS FUV spectra. Building on CALCOS, FaintCOS offers (1) a streamlined customization of CALCOS reduction parameters, (2) accurate dark current estimation with post-processed dark frames (Worseck et al. 2016), and (3) science-grade co-addition of sub-exposures across different COS wavelength settings and *HST* data sets that preserves COS Poisson counts, and calculates correct confidence intervals accounting for the background (Feldman & Cousins 1998).

A.1. Optimized Detector Pulse Heights and Point Source Extraction Windows

FaintCOS reduces the impact of the dark current onto the extracted spectrum by employing custom pulse height amplitude (PHA) limits that reflect the state of the COS FUV detector at the time of observation, and by using narrow boxcar source extraction apertures that preserve the spectrophotometry of point sources. Boxcar extraction is adequate, because the more recent two-zone extraction algorithm (a boxcar with variable width) implemented in CALCOS is not applicable to dark frames.

The boxcar source extraction aperture was defined individually for every COS detector lifetime position, FUV grating,

central wavelength, and COS detector segment using the corrected event lists of standard stars⁵ recorded at high S/N. We analyzed their cross-dispersion profiles in 1 Å bins, and determined upper and lower corrected cross-dispersion detector coordinates y_{full} , which enclose 95% of the source counts in the bin. The total lowest and highest integer y_{full} of all bins determined the rectangular extraction aperture. We verified by eye that the apertures are sensible, disregarding the detector edges. In this way, $> 95\%$ of the light of a point source is included in the final apertures (Figure 14), while reducing the dark current by $\sim 40\%$ compared to the default CALCOS boxcar extraction windows. We found $< 10\%$ deviations of the trace position for different visits with the same setup, which can be explained by statistical fluctuations, round-off errors, or small pointing inaccuracies. While our optimized apertures are reasonable for point sources, the user can adjust them to the science objective.

FaintCOS also uses more rigorous PHA limits, as described by Syphers & Shull (2013) and Worseck et al. (2016). Due to detector gain sag and voltage increases the PHA limits of source counts evolve with time and should be adjusted accordingly in FaintCOS. The PHA limits can be estimated by examining the PHA distribution of external counts (source and geocoronal emission) in the extraction window (Worseck et al. 2016). Lowering the PHA range from the standard $2 \leq \text{PHA} \leq 23$ to the actual range of our science data $2 \leq \text{PHA} \leq 12$ reduced the dark current by another $\sim 35\%$ while retaining $> 99\%$ of the source counts.

⁵ WD 0308–565 (Programs 12426, 12806, 13353, 13932, 14910, 15367, 15384, 15458, 15535), WD 0947+857 and WD 1057+719 (Program 11897).

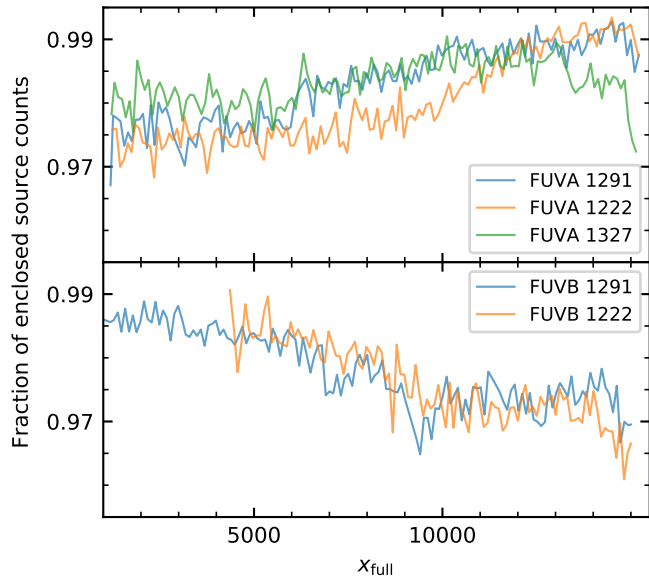


Figure 14. Fraction of source counts in the custom rectangular box-car extraction apertures in the dispersion direction on COS detector segments A and B for our used COS wavelength settings.

A.2. Accurate Estimation of the COS Dark Current

The COS FUV dark current is estimated from dark monitoring data taken within a user-specified time window (default is two months) around the observation date of the science data to capture the state of the FUV detector in terms of (1) gain sag due to illumination and (2) dark current variation due to varying environmental conditions (Worseck et al. 2016).

To account for the spatial and temporal variations in the FUV detector dark current, *FaintCOS* uses the PHA distribution in unilluminated parts of the detector that is sensitive to the environmental conditions (thermospheric density, cosmic ray hit rate) that vary with solar activity and geomagnetic latitude (Worseck et al. 2016). A subset of dark frames taken in similar conditions as the science exposure is selected by comparing the respective cumulative PHA distributions obtained from two predefined calibration windows above and below the science extraction aperture. Regions around geocoronal emission lines are excluded to avoid a change of the PHA distribution by scattered light. We selected dark frames whose normalized cumulative PHA distribution have a maximum absolute difference $D < 0.03$ with respect to the PHA distribution of the science exposure. The threshold D was increased if fewer than 5 dark frames were selected. Both D and the minimum number of dark frames can be set by the user according to the variability of solar activity and the availability of dark frames.

The final sample of dark frames is stacked and shifted to the focal-plane offset position of the science exposure. In the stack, the dark current is extracted from the science aperture, and smoothed with a running average. We chose a 500-pixel wide window that results in a robust estimate of the dark current including its spatial structure (Appendix B). Pixels with

data quality flags > 0 are excluded from the running average due to spatial or temporal detector issues. The systematic error of the averaged dark current is estimated with a Poisson standard deviation $\sqrt{N_{\text{dark}}}$, where N_{dark} is the number of counts in the averaging window. The smoothed dark current and its error are scaled to the science exposure using the total number of counts in the calibration windows, yielding the final dark current estimate B_{dark} and its error σ_{dark} .

A.3. COS Flat-Fielding and Flux Calibration

In contrast to *CALCOS*, *FaintCOS* preserves Poisson counts in co-added spectra, which in turn requires the storage of flat-field and flux calibration curves for every sub-exposure. The combined flat-field and deadtime correction K_{FF} is calculated from the corrected net count rate and the gross count rate provided by *CALCOS* in the extracted sub-exposures. Individual values are linearly interpolated to provide a continuous flat-field curve. The net count rate and the *CALCOS* flux values yield the flux calibration curve.

A.4. Subtraction of Scattered Geocoronal Ly α Emission

Scattered geocoronal Ly α emission in G140L spectra is modeled and subtracted following Worseck et al. (2016). The model predicts the corresponding counts $B_{\text{Ly}\alpha}$ and their associated error for data taken at the G140L central wavelengths 800 Å and 1105 Å. The 1280 Å setting cannot be corrected, because Ly α emission falls into the detector gap. For the G130M grating the sparse geocoronal calibration data sets are insufficient to model scattered geocoronal Ly α emission. From our deep G130M data we conclude that scattered geocoronal Ly α is negligible (Section 2.2).

A.5. Co-addition of Spectra Combining Central Wavelength Settings and Data Sets

Several custom routines have been developed to co-add COS exposures taken at several focal-plane offset positions, wavelength settings and/or in several visits. Peoples et al. (2017) list common implementations (Danforth et al. 2010; Keeney et al. 2012; Wakker et al. 2015; Tumlinson et al. 2013), and describe their own approach used for the *HST* Spectroscopic Legacy Archive. We find that all these routines are not fully applicable because they either (1) do not preserve Poisson counts, (2) overestimate statistical errors that must be calculated only for the signal part of the Poisson counts (Feldman & Cousins 1998), or (3) do not properly handle data quality flags.

In *FaintCOS*, exposures taken at different focal-plane offsets, central wavelengths and/or in several visits are co-added in count space on a regular wavelength grid. As the resolving power depends on wavelength, central wavelength, and the COS Lifetime Position, the bin size can be set by the user. In every bin, the pixel exposure time, gross counts, and the smoothed total background are summed across all sub-exposures. Only pixels with valid science data (data quality flag of zero) contribute to the final co-add. Flux calibration and flat-field curves are weighted with the exposure

Table 6. FITS table columns of the final co-added spectrum.

Column Name	Data Type	Units	Description
WAVELENGTH	float	Å	Wavelength
FLUX	float	erg s ⁻¹ cm ⁻² Å ⁻¹	Flux density f_λ (Equation A2)
FLUX_ERR_UP	float	erg s ⁻¹ cm ⁻² Å ⁻¹	Upper uncertainty for the flux density ^a
FLUX_ERR_DOWN	float	erg s ⁻¹ cm ⁻² Å ⁻¹	Lower uncertainty for the flux density ^a
GCOUNTS	integer	counts	Gross counts N
BACKGROUND	float	counts	Total background $B = B_{\text{dark}} + B_{\text{Ly}\alpha}$
BKG_ERR_UP	float	counts	Upper background error $\sigma_{B,\text{up}} = \sqrt{\sigma_{\text{dark}}^2 + \sigma_{\text{Ly}\alpha,\text{up}}^2}$
BKG_ERR_DOWN	float	counts	Lower background error $\sigma_{B,\text{down}} = \sqrt{\sigma_{\text{dark}}^2 + \sigma_{\text{Ly}\alpha,\text{down}}^2}$
DARK_CURRENT	float	counts	Estimated dark current B_{dark}
DARK_CURRENT_ERR	float	counts	Dark current error σ_{dark}
EXPTIME	float	seconds	Exposure time t_{exp}
DQ	integer		Data quality flag ^b
CALIB	float	counts cm ² Å erg ⁻¹	Flux calibration curve C
FLAT_CORR	float		Flatfield correction factor K_{FF}
LYA_SCATTER	float	counts	Scattered geocoronal Ly α emission $B_{\text{Ly}\alpha}$
LYA_SCATTER_ERR_UP	float	counts	Upper error $\sigma_{\text{Ly}\alpha,\text{up}}$ of $B_{\text{Ly}\alpha}$
LYA_SCATTER_ERR_DOWN	float	counts	Lower error $\sigma_{\text{Ly}\alpha,\text{down}}$ of $B_{\text{Ly}\alpha}$

^aThe sum of lower and upper uncertainty give a double-sided Poisson 1σ uncertainty corresponding to an 68.26% confidence level. Methods are either frequentist (Feldman & Cousins 1998) augmented by Monte Carlo simulations for $N < B$, or Bayesian (Kraft et al. 1991, shortest 68.26% confidence interval around posterior maximum).

^bLowest DQ value of all co-added counts in the wavelength bin adopted from CALCOS. DQ= 0 indicates no anomalies.

time. This is particularly important when combining different central wavelength settings that map parts of the wavelength range onto different COS detector segments.

The background error propagation needs to be treated carefully, since neighboring pixels of the same exposure are highly covariant due to the running average method used for the dark current estimation. The covariance is assumed to be negligible for different exposures. Thus, the total systematic background error is

$$\sigma_B = \sqrt{\sum_k \left(\sum_{i=1}^m \sigma_B^{ki} \right)^2}, \quad (\text{A1})$$

where exposure k contributes m pixels to the rebinned spectrum. The flux density per wavelength bin is calculated as

$$f_\lambda = \frac{(N - B)}{t_{\text{exp}} C K_{\text{FF}}}, \quad (\text{A2})$$

with gross counts N , background counts B , pixel exposure time t_{exp} , flux calibration curve C , and correction factor K_{FF} . The final co-added spectrum is stored in the output table `OBJECT_spectrum.fits` described in Table 6.

B. VALIDATION OF THE DARK CURRENT MODEL

We tested our advanced dark subtraction technique by treating dark frames as science data. The corrected event lists of individual science exposures ($t_{\text{exp}} = 2000\text{--}2900$ s) were replaced with those of two randomly selected 1330 s dark exposures taken in a two months period around the observation date. The validation data created in this way were run through our dark current estimation and co-adding routines.

Figure 15 shows the results obtained for 200 realizations of the combined data set on HE2QS J1630+0435 (Table 1). The total exposure time of each validation data set (42,560 s) is comparable to the science exposure time (45,915 s). We measured the deviation $N/B - 1$ between the measured counts N and estimated dark current model B in 1 Å bins (25 pixels). On average the dark current is slightly underestimated by $\lesssim 0.5\%$ (Figure 15, lower right panel), with localized larger deviations. The small-scale underestimation at 1220 Å is likely due to gain sag around geocoronal Ly α that is not captured by our 500-pixel running average. Other deviations are less obvious due to the different pixel exposure times, especially at the ends of the spectral range and due to the extrapolation of the smoothed dark at the detector edges. However, the deviations are completely dominated by Poisson noise around the estimated dark current. The majority of

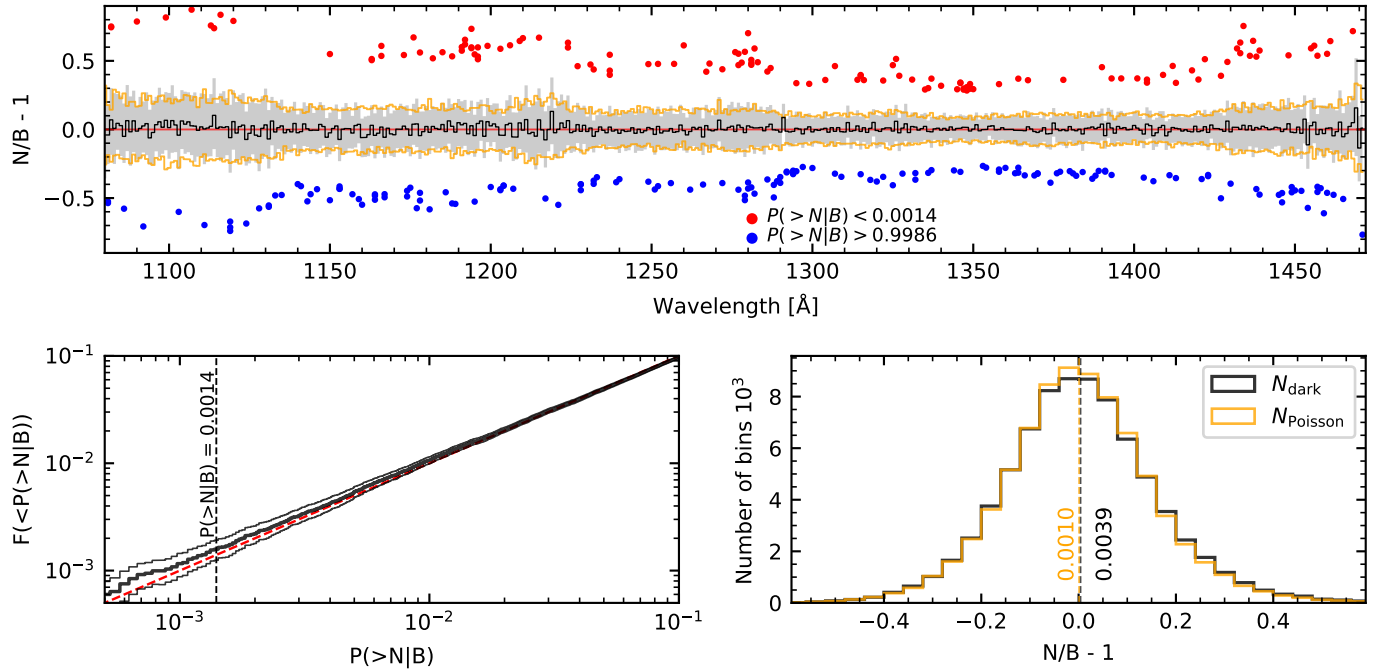


Figure 15. Results of our dark subtraction tests using subsets of darks as data. *Upper panel:* Average deviation $N/B - 1$ in 1 \AA bins from 200 realizations (black) and estimated 1σ scatter of the distribution (gray). Red and blue points show individual 3σ deviations with $P(> N|B) \leq 0.0014$ and $P(> N|B) \geq 0.9986$, respectively. The orange lines indicate the 1σ scatter of purely Poisson distributed counts N_{Poisson} assuming the background model B . *Lower left panel:* Cumulative fraction of Poisson probabilities per 1 \AA bin for measured counts N (thick black) and its 2σ statistical error (thin black). The dashed red and black lines show identity and $P(> N|B) = 0.0014$, respectively. *Lower right panel:* Histogram of deviations $N/B - 1$ in 1 \AA bins for measured counts N_{dark} and Poisson distributed counts N_{Poisson} according to our modeled dark. The dashed lines show the respective average.

the bins show a very low average deviation of $\leq 5\%$ which is comparable to the estimated systematic dark current error of 1–6%. The fraction of bins with Poisson probability $P \leq 0.0014$ (3σ), which would indicate pixels with statistically significant transmission in the scientific data, is slightly higher than expected for purely Poisson distributed counts (Figure 15, lower left panel). This effect can be explained with our slight underestimation of the dark current and its small-scale structure on the detector below our 500-pixel averaging scale.

C. DECONTAMINATION FROM GEOCORONAL EMISSION LINES

To verify the tentatively detected He II Ly β transmission coinciding with the geocoronal N I $\lambda 1200$ emission line (Figure 2), we extensively tested the time variation of the geocoronal N I $\lambda 1200$ and O I $\lambda 1304$ emission lines. Often it is possible to entirely suppress these two emission lines in the affected wavelength ranges by considering only part of the data taken during orbital night. We tested the correlation of the geocoronal line fluxes during orbital night in archival *HST*/COS blank-sky observations⁶. We reduced the blank-sky sets covering both N I and O I in the same way as our

science data, restricting the data in the vicinity of the lines to night-only data. We calculated the probability $P(> N|B)$ (Equation 1) to find at least N counts given the background B in the N I (1198.5–1201.0 Å) and O I (1301–1307 Å) regions. Low P values correspond to significant flux.

Figure 16 shows the resulting P_{NI} and P_{OI} of each blank-sky data set in comparison to the same values for individual science data sets. The plot can be divided into four regions for the four possible scenarios assuming a 3σ ($P(> N|B) = 0.0014$) detection limit: (1) no significant flux in both regions, (2) strong (weak/insignificant) flux in the O I (N I) region, (3) significant flux in both regions, and (4) insignificant flux in the O I region, but significant flux in the N I region. Scenario 4 is very rare for the blank-sky data sets given the 1σ errors of the P values estimated from the systematic background error, so significant N I emission is generally accompanied by strong O I emission. The HE2QS J2311–1417 data sets are consistently in Scenario 1, showing no residuals in N I and O I. For all but two HE2QS J1630+0435 data sets it is highly unlikely that the residual flux is geocoronal N I, because O I is effectively eliminated. The two high P_{NI} values are caused by the short exposure time of these particular HE2QS J1630+0435 data sets. Thus, we conclude that the residual flux at 1200 Å in the spectrum of HE2QS J1630+0435 is probably He II Ly β transmission (Figure 2), but due to the fact that all blank-

⁶ <https://www.stsci.edu/hst/instrumentation/cos/calibration/airglow>

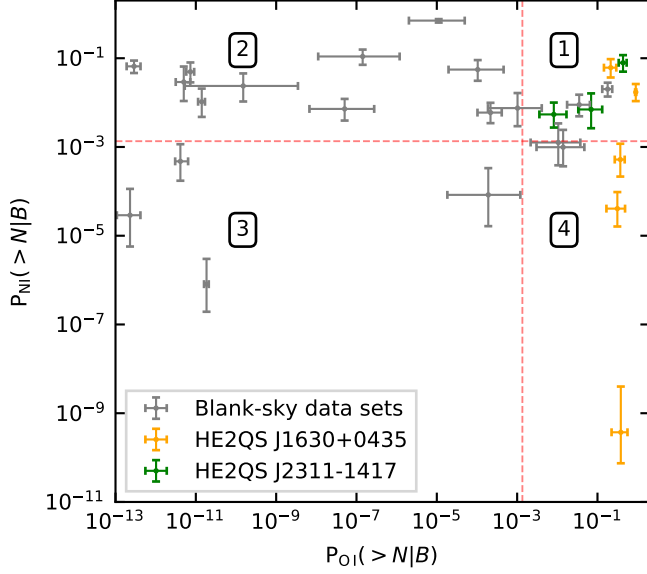


Figure 16. Probability P (Equation 1) to measure N counts in the spectral ranges of geocoronal N I and O I during orbital night given the background B . Blank-sky data sets and individual science data sets are shown in gray and color, respectively. The red dashed lines indicate a 3σ detection at $P(> N|B) = 0.0014$. The errors were calculated by varying the background according to the systematic background error.

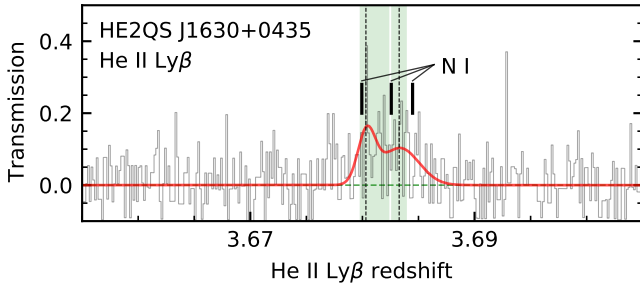


Figure 17. Similar to Figure 9 but for He II Ly β in the spectrum of HE2QS J1630+0435. Thick vertical lines indicate the position of the geocoronal N I λ 1200 triplet.

sky observations are very short (orbital night < 1200 s) we cannot definitely determine the origin of the flux. Much longer exposures might show residuals comparable to the flux detected in our science data, and we hesitate to draw general conclusions from the successful decontamination of our HE2QS J2311–1417 data sets.

D. TENTATIVE HE II LY β TRANSMISSION AT $Z \approx 3.68$

Here we consider the case where the flux at 1200 \AA in the spectrum of HE2QS J1630+0435 is not residual geocoronal N I, but instead intergalactic He II Ly β transmission. Figure 17 shows its decomposition into two Gaussian components with fit parameters ($z_{\beta,m}, \sigma_m, A_m$) of $(3.6803, 50 \text{ km s}^{-1}, 0.142)$ and $(3.6833, 109 \text{ km s}^{-1}, 0.103)$,

respectively. Following our procedure for the combined posterior in Section 5.3, we use the occurrence of these two He II Ly β and two He II Ly α spike components to infer a He II photoionization rate $\Gamma_{\text{HeII}} = (2.5^{+0.7}_{-0.6}) \times 10^{-15} \text{ s}^{-1}$ at $z = 3.56\text{--}3.72$ in the HE2QS J1630+0435 sightline. This photoionization rate is consistent with our inferences from He II Ly α and He II Ly β at $z \sim 3.6$ at 2σ .

REFERENCES

- Almgren, A. S., Bell, J. B., Lijewski, M. J., Lukić, Z., & Van Andel, E. 2013, *ApJ*, 765, 39, doi: [10.1088/0004-637X/765/1/39](https://doi.org/10.1088/0004-637X/765/1/39)
- Astropy Collaboration, Robitaille, T. P., Tollerud, E. J., et al. 2013, *A&A*, 558, A33, doi: [10.1051/0004-6361/201322068](https://doi.org/10.1051/0004-6361/201322068)
- Astropy Collaboration, Price-Whelan, A. M., Sipőcz, B. M., et al. 2018, *AJ*, 156, 123, doi: [10.3847/1538-3881/aabc4f](https://doi.org/10.3847/1538-3881/aabc4f)
- Bañados, E., Venemans, B. P., Mazzucchelli, C., et al. 2018, *Nature*, 553, 473, doi: [10.1038/nature25180](https://doi.org/10.1038/nature25180)
- Barnett, R., Warren, S. J., Becker, G. D., et al. 2017, *A&A*, 601, A16, doi: [10.1051/0004-6361/201630258](https://doi.org/10.1051/0004-6361/201630258)
- Becker, G. D., Bolton, J. S., Haehnelt, M. G., & Sargent, W. L. W. 2011, *MNRAS*, 410, 1096, doi: [10.1111/j.1365-2966.2010.17507.x](https://doi.org/10.1111/j.1365-2966.2010.17507.x)
- Becker, G. D., Bolton, J. S., Madau, P., et al. 2015, *MNRAS*, 447, 3402, doi: [10.1093/mnras/stu2646](https://doi.org/10.1093/mnras/stu2646)
- Becker, R. H., Fan, X., White, R. L., et al. 2001, *AJ*, 122, 2850, doi: [10.1086/324231](https://doi.org/10.1086/324231)
- Boera, E., Becker, G. D., Bolton, J. S., & Nasir, F. 2019, *ApJ*, 872, 101, doi: [10.3847/1538-4357/aafee4](https://doi.org/10.3847/1538-4357/aafee4)
- Boera, E., Murphy, M. T., Becker, G. D., & Bolton, J. S. 2014, *MNRAS*, 441, 1916, doi: [10.1093/mnras/stu660](https://doi.org/10.1093/mnras/stu660)
- Bosman, S. E. I., Fan, X., Jiang, L., et al. 2018, *MNRAS*, 479, 1055, doi: [10.1093/mnras/sty1344](https://doi.org/10.1093/mnras/sty1344)
- Cardelli, J. A., Clayton, G. C., & Mathis, J. S. 1989, *ApJ*, 345, 245, doi: [10.1086/167900](https://doi.org/10.1086/167900)
- Chardin, J., Haehnelt, M. G., Bosman, S. E. I., & Puchwein, E. 2018, *MNRAS*, 473, 765, doi: [10.1093/mnras/stx2362](https://doi.org/10.1093/mnras/stx2362)
- Choudhury, T. R., Paranjape, A., & Bosman, S. E. I. 2021, *MNRAS*, doi: [10.1093/mnras/stab045](https://doi.org/10.1093/mnras/stab045)
- Compostella, M., Cantalupo, S., & Porciani, C. 2013, *MNRAS*, 435, 3169, doi: [10.1093/mnras/stt1510](https://doi.org/10.1093/mnras/stt1510)
- . 2014, *MNRAS*, 445, 4186, doi: [10.1093/mnras/stu2035](https://doi.org/10.1093/mnras/stu2035)
- Croft, R. A. C., Weinberg, D. H., Katz, N., & Hernquist, L. 1997, *ApJ*, 488, 532, doi: [10.1086/304723](https://doi.org/10.1086/304723)
- Danforth, C. W., Keeney, B. A., Stocke, J. T., Shull, J. M., & Yao, Y. 2010, *ApJ*, 720, 976, doi: [10.1088/0004-637X/720/1/976](https://doi.org/10.1088/0004-637X/720/1/976)
- Davies, F. B., Furlanetto, S. R., & Dixon, K. L. 2017, *MNRAS*, 465, 2886, doi: [10.1093/mnras/stw2868](https://doi.org/10.1093/mnras/stw2868)
- Davies, F. B., Hennawi, J. F., Eilers, A.-C., & Lukić, Z. 2018, *ApJ*, 855, 106, doi: [10.3847/1538-4357/aaaf70](https://doi.org/10.3847/1538-4357/aaaf70)
- Eilers, A.-C., Davies, F. B., & Hennawi, J. F. 2018, *ApJ*, 864, 53, doi: [10.3847/1538-4357/aad4fd](https://doi.org/10.3847/1538-4357/aad4fd)
- Eilers, A.-C., Hennawi, J. F., Davies, F. B., & Oñorbe, J. 2019, *ApJ*, 881, 23, doi: [10.3847/1538-4357/ab2b3f](https://doi.org/10.3847/1538-4357/ab2b3f)
- Fan, X., Strauss, M. A., Becker, R. H., et al. 2006, *AJ*, 132, 117, doi: [10.1086/504836](https://doi.org/10.1086/504836)
- Fardal, M. A., Giroux, M. L., & Shull, J. M. 1998, *AJ*, 115, 2206, doi: [10.1086/300359](https://doi.org/10.1086/300359)
- Feldman, G. J., & Cousins, R. D. 1998, *PhRvD*, 57, 3873, doi: [10.1103/PhysRevD.57.3873](https://doi.org/10.1103/PhysRevD.57.3873)
- Furlanetto, S. R., & Dixon, K. L. 2010, *ApJ*, 714, 355, doi: [10.1088/0004-637X/714/1/355](https://doi.org/10.1088/0004-637X/714/1/355)
- Furlanetto, S. R., & Oh, S. P. 2008, *ApJ*, 681, 1, doi: [10.1086/588546](https://doi.org/10.1086/588546)
- . 2009, *ApJ*, 701, 94, doi: [10.1088/0004-637X/701/1/94](https://doi.org/10.1088/0004-637X/701/1/94)
- Gaikwad, P., Rauch, M., Haehnelt, M. G., et al. 2020, *MNRAS*, 494, 5091, doi: [10.1093/mnras/staa907](https://doi.org/10.1093/mnras/staa907)
- Gallerani, S., Choudhury, T. R., & Ferrara, A. 2006, *MNRAS*, 370, 1401, doi: [10.1111/j.1365-2966.2006.10553.x](https://doi.org/10.1111/j.1365-2966.2006.10553.x)
- Gallerani, S., Ferrara, A., Fan, X., & Choudhury, T. R. 2008, *MNRAS*, 386, 359, doi: [10.1111/j.1365-2966.2008.13029.x](https://doi.org/10.1111/j.1365-2966.2008.13029.x)
- Garaldi, E., Compostella, M., & Porciani, C. 2019a, *MNRAS*, 483, 5301, doi: [10.1093/mnras/sty3414](https://doi.org/10.1093/mnras/sty3414)
- Garaldi, E., Gnedin, N. Y., & Madau, P. 2019b, *ApJ*, 876, 31, doi: [10.3847/1538-4357/ab12dc](https://doi.org/10.3847/1538-4357/ab12dc)
- Gnedin, N. Y., Becker, G. D., & Fan, X. 2017, *ApJ*, 841, 26, doi: [10.3847/1538-4357/aa6c24](https://doi.org/10.3847/1538-4357/aa6c24)
- Green, J. C., Froning, C. S., Osterman, S., et al. 2012, *ApJ*, 744, 60, doi: [10.1088/0004-637X/744/1/60](https://doi.org/10.1088/0004-637X/744/1/60)
- Gunn, J. E., & Peterson, B. A. 1965, *ApJ*, 142, 1633, doi: [10.1086/148444](https://doi.org/10.1086/148444)
- Haardt, F., & Madau, P. 2012, *ApJ*, 746, 125, doi: [10.1088/0004-637X/746/2/125](https://doi.org/10.1088/0004-637X/746/2/125)
- Heap, S. R., Williger, G. M., Smette, A., et al. 2000, *ApJ*, 534, 69, doi: [10.1086/308719](https://doi.org/10.1086/308719)
- Hiss, H., Walther, M., Hennawi, J. F., et al. 2018, *ApJ*, 865, 42, doi: [10.3847/1538-4357/aada86](https://doi.org/10.3847/1538-4357/aada86)
- Hunter, J. D. 2007, *Computing in Science and Engineering*, 9, 90, doi: [10.1109/MCSE.2007.55](https://doi.org/10.1109/MCSE.2007.55)
- Jakobsen, P., Boksenberg, A., Deharveng, J. M., et al. 1994, *Nature*, 370, 35, doi: [10.1038/370035a0](https://doi.org/10.1038/370035a0)
- Jakobsen, P., Jansen, R. A., Wagner, S., & Reimers, D. 2003, *A&A*, 397, 891, doi: [10.1051/0004-6361:20021579](https://doi.org/10.1051/0004-6361:20021579)
- Keating, L. C., Kulkarni, G., Haehnelt, M. G., Chardin, J., & Aubert, D. 2020a, *MNRAS*, 497, 906, doi: [10.1093/mnras/staa1909](https://doi.org/10.1093/mnras/staa1909)
- Keating, L. C., Weinberger, L. H., Kulkarni, G., et al. 2020b, *MNRAS*, 491, 1736, doi: [10.1093/mnras/stz3083](https://doi.org/10.1093/mnras/stz3083)
- Keeney, B. A., Danforth, C. W., Stocke, J. T., France, K., & Green, J. C. 2012, *PASP*, 124, 830, doi: [10.1086/667392](https://doi.org/10.1086/667392)
- Khrykin, I. S., Hennawi, J. F., & Worseck, G. 2019, *MNRAS*, 484, 3897, doi: [10.1093/mnras/stz135](https://doi.org/10.1093/mnras/stz135)
- Kraft, R. P., Burrows, D. N., & Nousek, J. A. 1991, *ApJ*, 374, 344, doi: [10.1086/170124](https://doi.org/10.1086/170124)
- Kulkarni, G., Keating, L. C., Haehnelt, M. G., et al. 2019a, *MNRAS*, 485, L24, doi: [10.1093/mnras/rlz025](https://doi.org/10.1093/mnras/rlz025)

- Kulkarni, G., Worseck, G., & Hennawi, J. F. 2019b, *MNRAS*, 488, 1035, doi: [10.1093/mnras/stz1493](https://doi.org/10.1093/mnras/stz1493)
- La Plante, P., Trac, H., Croft, R., & Cen, R. 2017, *ApJ*, 841, 87, doi: [10.3847/1538-4357/aa7136](https://doi.org/10.3847/1538-4357/aa7136)
- Lidz, A., Faucher-Giguère, C.-A., Dall'Aglio, A., et al. 2010, *ApJ*, 718, 199, doi: [10.1088/0004-637X/718/1/199](https://doi.org/10.1088/0004-637X/718/1/199)
- Lukić, Z., Stark, C. W., Nugent, P., et al. 2015, *MNRAS*, 446, 3697, doi: [10.1093/mnras/stu2377](https://doi.org/10.1093/mnras/stu2377)
- Madau, P., & Meiksin, A. 1994, *ApJL*, 433, L53, doi: [10.1086/187546](https://doi.org/10.1086/187546)
- Martin, D. C., Fanson, J., Schiminovich, D., et al. 2005, *ApJL*, 619, L1, doi: [10.1086/426387](https://doi.org/10.1086/426387)
- McGreer, I. D., Mesinger, A., & D'Odorico, V. 2015, *MNRAS*, 447, 499, doi: [10.1093/mnras/stu2449](https://doi.org/10.1093/mnras/stu2449)
- McQuinn, M. 2009, *ApJL*, 704, L89, doi: [10.1088/0004-637X/704/2/L89](https://doi.org/10.1088/0004-637X/704/2/L89)
- McQuinn, M., Lidz, A., Zaldarriaga, M., et al. 2009, *ApJ*, 694, 842, doi: [10.1088/0004-637X/694/2/842](https://doi.org/10.1088/0004-637X/694/2/842)
- Meiksin, A. 2020, *MNRAS*, 491, 4884, doi: [10.1093/mnras/stz3395](https://doi.org/10.1093/mnras/stz3395)
- Miralda-Escude, J. 1993, *MNRAS*, 262, 273, doi: [10.1093/mnras/262.1.273](https://doi.org/10.1093/mnras/262.1.273)
- Miralda-Escudé, J., Haehnelt, M., & Rees, M. J. 2000, *ApJ*, 530, 1, doi: [10.1086/308330](https://doi.org/10.1086/308330)
- Møller, P., & Jakobsen, P. 1990, *A&A*, 228, 299
- Morrissey, P., Conrow, T., Barlow, T. A., et al. 2007, *ApJS*, 173, 682, doi: [10.1086/520512](https://doi.org/10.1086/520512)
- Murthy, J. 2014, *ApJS*, 213, 32, doi: [10.1088/0067-0049/213/2/32](https://doi.org/10.1088/0067-0049/213/2/32)
- Nasir, F., & D'Aloisio, A. 2020, *MNRAS*, 494, 3080, doi: [10.1093/mnras/staa894](https://doi.org/10.1093/mnras/staa894)
- Oñorbe, J., Hennawi, J. F., & Lukić, Z. 2017, *ApJ*, 837, 106, doi: [10.3847/1538-4357/aa6031](https://doi.org/10.3847/1538-4357/aa6031)
- Oh, S. P., & Furlanetto, S. R. 2005, *ApJL*, 620, L9, doi: [10.1086/428610](https://doi.org/10.1086/428610)
- Paschos, P., & Norman, M. L. 2005, *ApJ*, 631, 59, doi: [10.1086/431787](https://doi.org/10.1086/431787)
- Peebles, M., Tumlinson, J., Fox, A., et al. 2017, *The Hubble Spectroscopic Legacy Archive, Instrument Science Report COS 2017-4*
- Picard, A., & Jakobsen, P. 1993, *A&A*, 276, 331
- Planck Collaboration, Aghanim, N., Akrami, Y., et al. 2018, *arXiv e-prints*, arXiv:1807.06209. <https://arxiv.org/abs/1807.06209>
- Puchwein, E., Haardt, F., Haehnelt, M. G., & Madau, P. 2019, *MNRAS*, 485, 47, doi: [10.1093/mnras/stz222](https://doi.org/10.1093/mnras/stz222)
- Reimers, D., Kohler, S., Wisotzki, L., et al. 1997, *A&A*, 327, 890. <https://arxiv.org/abs/astro-ph/9707173>
- Ricotti, M., Gnedin, N. Y., & Shull, J. M. 2000, *ApJ*, 534, 41, doi: [10.1086/308733](https://doi.org/10.1086/308733)
- Schaye, J., Theuns, T., Rauch, M., Efstathiou, G., & Sargent, W. L. W. 2000, *MNRAS*, 318, 817, doi: [10.1046/j.1365-8711.2000.03815.x](https://doi.org/10.1046/j.1365-8711.2000.03815.x)
- Schlegel, D. J., Finkbeiner, D. P., & Davis, M. 1998, *ApJ*, 500, 525, doi: [10.1086/305772](https://doi.org/10.1086/305772)
- Schmidt, T. M., Hennawi, J. F., Worseck, G., et al. 2018, *ApJ*, 861, 122, doi: [10.3847/1538-4357/aac8e4](https://doi.org/10.3847/1538-4357/aac8e4)
- Schmidt, T. M., Worseck, G., Hennawi, J. F., Prochaska, J. X., & Crighton, N. H. M. 2017, *ApJ*, 847, 81, doi: [10.3847/1538-4357/aa83ac](https://doi.org/10.3847/1538-4357/aa83ac)
- Shull, J. M., France, K., Danforth, C. W., Smith, B., & Tumlinson, J. 2010, *ApJ*, 722, 1312, doi: [10.1088/0004-637X/722/2/1312](https://doi.org/10.1088/0004-637X/722/2/1312)
- Smette, A., Heap, S. R., Williger, G. M., et al. 2002, *ApJ*, 564, 542, doi: [10.1086/324397](https://doi.org/10.1086/324397)
- Sokasian, A., Abel, T., & Hernquist, L. 2002, *MNRAS*, 332, 601, doi: [10.1046/j.1365-8711.2002.05291.x](https://doi.org/10.1046/j.1365-8711.2002.05291.x)
- Songaila, A., & Cowie, L. L. 2002, *AJ*, 123, 2183, doi: [10.1086/340079](https://doi.org/10.1086/340079)
- Sternberg, A. 1989, *ApJ*, 347, 863, doi: [10.1086/168177](https://doi.org/10.1086/168177)
- Syphers, D., Anderson, S. F., Zheng, W., et al. 2009a, *ApJS*, 185, 20, doi: [10.1088/0067-0049/185/1/20](https://doi.org/10.1088/0067-0049/185/1/20)
- . 2012, *AJ*, 143, 100, doi: [10.1088/0004-6256/143/4/100](https://doi.org/10.1088/0004-6256/143/4/100)
- Syphers, D., & Shull, J. M. 2013, *ApJ*, 765, 119, doi: [10.1088/0004-637X/765/2/119](https://doi.org/10.1088/0004-637X/765/2/119)
- . 2014, *ApJ*, 784, 42, doi: [10.1088/0004-637X/784/1/42](https://doi.org/10.1088/0004-637X/784/1/42)
- Syphers, D., Anderson, S. F., Zheng, W., et al. 2009b, *ApJ*, 690, 1181, doi: [10.1088/0004-637X/690/2/1181](https://doi.org/10.1088/0004-637X/690/2/1181)
- . 2011, *ApJ*, 742, 99, doi: [10.1088/0004-637X/742/2/99](https://doi.org/10.1088/0004-637X/742/2/99)
- The LUVUOIR Team. 2019, *arXiv e-prints*, arXiv:1912.06219. <https://arxiv.org/abs/1912.06219>
- Tumlinson, J., Thom, C., Werk, J. K., et al. 2013, *ApJ*, 777, 59, doi: [10.1088/0004-637X/777/1/59](https://doi.org/10.1088/0004-637X/777/1/59)
- van der Walt, S., Colbert, S. C., & Varoquaux, G. 2011, *Computing in Science and Engineering*, 13, 22, doi: [10.1109/MCSE.2011.37](https://doi.org/10.1109/MCSE.2011.37)
- Virtanen, P., Gommers, R., Oliphant, T. E., et al. 2020, *Nature Methods*, 17, 261, doi: [10.1038/s41592-019-0686-2](https://doi.org/10.1038/s41592-019-0686-2)
- Wakker, B. P., Hernandez, A. K., French, D. M., et al. 2015, *ApJ*, 814, 40, doi: [10.1088/0004-637X/814/1/40](https://doi.org/10.1088/0004-637X/814/1/40)
- Walther, M., Oñorbe, J., Hennawi, J. F., & Lukić, Z. 2019, *ApJ*, 872, 13, doi: [10.3847/1538-4357/aafad1](https://doi.org/10.3847/1538-4357/aafad1)
- White, R. L., Becker, R. H., Fan, X., & Strauss, M. A. 2003, *AJ*, 126, 1, doi: [10.1086/375547](https://doi.org/10.1086/375547)
- Worseck, G., Davies, F. B., Hennawi, J. F., & Prochaska, J. X. 2019, *ApJ*, 875, 111, doi: [10.3847/1538-4357/ab0fa1](https://doi.org/10.3847/1538-4357/ab0fa1)
- Worseck, G., & Prochaska, J. X. 2011, *ApJ*, 728, 23, doi: [10.1088/0004-637X/728/1/23](https://doi.org/10.1088/0004-637X/728/1/23)
- Worseck, G., Prochaska, J. X., Hennawi, J. F., & McQuinn, M. 2016, *ApJ*, 825, 144, doi: [10.3847/0004-637X/825/2/144](https://doi.org/10.3847/0004-637X/825/2/144)
- Worseck, G., Prochaska, J. X., McQuinn, M., et al. 2011, *ApJL*, 733, L24, doi: [10.1088/2041-8205/733/2/L24](https://doi.org/10.1088/2041-8205/733/2/L24)

Yang, J., Wang, F., Fan, X., et al. 2020, arXiv e-prints,
arXiv:2009.13544. <https://arxiv.org/abs/2009.13544>

Zheng, W., Kriss, G. A., Deharveng, J. M., et al. 2004, ApJ, 605,
631, doi: [10.1086/382498](https://doi.org/10.1086/382498)